Magma-fluid interactions beneath the Akutan Volcano in Aleutian Arc based on the results of local earthquake tomography

Koulakov Ivan[1], Komzeleva Viktoria[2], Smirnov Sergey Z.[3], and Bortnikova Svetlana B.[2]

[1]Trofimuk Institute of Petroleum Geology and Geophysics, SB RAS
[2]Trofimuk Institute of Petroleum Geology and Geophysics SB RAS
[3]Sobolev Institute of Geology and Mineralogy SB RAS

November 16, 2022

Abstract

Akutan Island hosts a volcano considered as one of most active in the Aleutians Arc. Besides the regular eruption activity, Akutan in 1996 experienced a remarkable seismic unrest with earthquakes reaching the magnitude of M 5.3. We build a new tomography model including the 3D distributions of the , and ratio based on arrival time data from more than 4000 local earthquakes. In this model, we reveal a columnar anomaly of high ratio with the top boundary at a depth of 5-6 km below surface, which represents a steady conduit feeding the Akutan volcano. At a depth of ~4 km, the deep conduit is split in two branches, one of which ascend to the summit area and another one directs to a fumarole field at the flank of the volcano. This structure explains distinct geochemical features of emitted gases in these two areas. In the upper part of the velocity model, the highly heterogeneous structures are associated with interactions of shallow magmatic sources, meteoric and magmatic fluids, as well as degassing. Besides the prominent anomaly associated with the shallow magma reservoir beneath the caldera and the active cone, we observe several areas with high ratio, some of which are interpreted as shallow magma storages, and some as zones of meteoric water penetration. We propose a scenario of abrupt fluid ejection from the deep magma conduit that led to the seismic unrest and strong ground deformations in the Akutan area in 1996.

Magma-fluid interactions beneath the Akutan Volcano in Aleutian Arc based on the results of local earthquake tomography

by

Ivan Koulakov[1,2,3], Viktoria Komzeleva[1,4], Sergey Z. Smirnov[5] and Svetlana B. Bortnikova[1]

* Corresponding author: email: KoulakovIY@ipgg.sbras.ru

1. Trofimuk Institute of Petroleum Geology and Geophysics SB RAS, Prospekt Koptyuga, 3, 630090, Novosibirsk, Russia (KoulakovIY@ipgg.sbras.ru, BortnikovaSB@ipgg.sbras.ru).

2. Novosibirsk State University, Novosibirsk, Russia, Pirogova 2, 630090, Novosibirsk, Russia

3. Institute of Volcanology and Seismology FEB RAS, Piip Boulevard, 9, 693006, Petropavlovsk-Kamchatsky, Russia.

4. Novosibirsk State Technical University, Karl Marks avenue 20, Novosibirsk, Russia, 630073. (vika.komzeleva@mail.ru).

5. Sobolev Institute of Geology and Mineralogy SB RAS, Prospekt Koptyuga, 3, Novosibirsk 630090, Russia (ssmr@igm.sbras.ru)

Citation: Koulakov I., V. Komzeleva, S.Z. Smirnov and S.B. Bortnikova (2020), Magma-fluid interactions beneath the Akutan Volcano in Aleutian Arc based on the results of local earthquake tomography, *Journal of Geophysical Research, Solid Earth* (submitted).

July 2020, Novosibirsk

Abstract

Akutan Island hosts a volcano considered as one of most active in the Aleutians Arc. Besides the regular eruption activity, Akutan in 1996 experienced a remarkable seismic unrest with earthquakes reaching the magnitude of M 5.3. We build a new tomography model including the 3D distributions of the *Vp*, *Vs* and *Vp/Vs* ratio based on arrival time data from more than 4000 local earthquakes. In this model, we reveal a columnar anomaly of high *Vp/Vs* ratio with the top boundary at a depth of 5-6 km below surface, which represents a steady conduit feeding the Akutan volcano. At a depth of ~4 km, the deep conduit is split in two branches, one of which ascend to the summit area and another one directs to a fumarole field at the flank of the volcano. This structure explains distinct geochemical features of emitted gases in these two areas. In the upper part of the velocity model, the highly heterogeneous structures are associated with interactions of shallow magmatic sources, meteoric and magmatic fluids, as well as degassing. Besides the prominent anomaly associated with the shallow magma reservoir beneath the caldera and the active cone, we observe several areas with high *Vp/Vs* ratio, some of which are interpreted as shallow magma storages, and some as zones of meteoric water penetration. We propose a scenario of abrupt fluid ejection from the deep magma conduit that led to the seismic unrest and strong ground deformations in the Akutan area in 1996.

Key words: Aleutian arc, Akutan volcano, seismic tomography, local seismicity, magma conduit, meteoric and magmatic fluids, seismic unrest

1. Introduction

Volcanoes in the Aleutian arc and Alaska are located in low-populated areas; nevertheless, they represent serious hazard to the local population and infrastructure, as well as to the air traffic along dense aviation routes in the northern Pacific (Casadevall, 1993). To enable fast detection of ongoing volcanic eruptions, most of active volcanoes in these regions are equipped with telemetric seismic networks that continuously transmit the records to the offices of the Alaskan Volcanological Observatory (AVO), where they are processed in real time (Dixon et al., 2019). Besides the hazard assessment, the data recorded by these networks are used for studying fundamental aspects of functioning magma plumbing systems, which still remain poorly understood due to their complexity. Mechanical, chemical and thermal interactions of materials in the magmatic systems require multidisciplinary approaches, in which geophysical imaging of structures beneath volcanoes is as one of the essential elements.

In this study, we investigate the upper- and middle-crustal structure beneath the Akutan Island located in the eastern part of the Aleutian arc (Figure 1a). This island hosts the Akutan volcano, which is one of the most active in the Aleutian arc, with dozens of documented eruptions starting from the eighteen century (Siebert, Simkin, 2013). These eruptions were mostly weak or moderate; however, the existence of a Holocene caldera with the diameter of ~2 km and thick scoria-bearing, lapilli tephra (Akutan tephra) widely spreading over the entire island surface (Waythomas, 1999) indicates that Akutan has a serious potential for explosive caldera-forming eruptions. During the past century, Akutan demonstrated variable styles of volcanic activity, such as lava flows, gas emissions and strombolian explosive eruptions ejecting ash plumes (e.g. Miller et al., 1998). The most recent eruption of Akutan occurred in 1992. However, after this, in March 1996, a remarkable seismic unrest occurred, which did not lead to a volcanic eruption, but caused earthquakes with the magnitudes of up to M5.3 and triggered strong ground deformations (Lu et al., 2000, 2005). These and other aspects of Akutan's activity are discussed in more details in the next section.

Seismic tomography is an efficient tool to reveal the geometry of the magmatic feeding systems that was successfully used to explore many volcanoes throughout the World. For example, volcanoes of the Aleutian Arc and Alaska have been investigated in a number of tomographic studies, such as those of Mount Spurr (Power et al., 1998; Koulakov et al., 2013, 2018), Mount Redoubt (Benz et al., 1996; Kasatkina et al., 2014), Katmai Group (Murphy et al., 2014), Okmok (Ohlendorf et al., 2014), Augustine (Syracuse et al., 2011), Atka (Koulakov et al., 2020), and each of them shed light to the feeding processes of the magmatic systems. It should be noted, that most of volcanoes are in some sense unique and not similar to others. Therefore, extrapolation of properties found for one volcano is not always suitable for another volcano, though of similar type. That is why every volcano requires individual investigations that contributes in understanding the general principles of functioning the magma feeding systems.

Another aspect of interest is possible exploration of geothermal resources in Akutan, which might serve as cheap and ecologically friendly energy for approximately 1000 inhabitants of the island (e.g., Mann et al., 2019). Within the program of geothermal energy exploiting, a series of multidisciplinary surveys were performed in the area of geothermal activity with the purpose of studying the roots of the hot springs and a fumarole area in the eastern part of the island (Bergfeld et al., 2014; Ohren et al., 2013, Mann et al., 2019). The geophysical part of the program included magnetotelluric (MT) and gravity studies in the Akutan Geothermal Project area, including Flank Fumarole and Hot Spring Bay Valley areas. It was found that the low-resistivity area, representing water-saturated rocks, is observed in a relatively shallow layer at depths down to 200-400 m. In deeper layers, this survey identified a high-resistivity anomaly, which is especially prominent beneath the Flank Fumarole zone. Several exploration boreholes in the Hot Spring Bay Valley reached the depths of 250 - 500 meters and discovered a zone of high permeability and strong temperature gradient marking the aquifer layers feeding the springs (Stelling et al., 2015, Mann et al., 2019). According to MT and gravity data by Ohren et al., (2013) the high-temperature hydrothermal source is likely located just beneath the Flank Fumarole area above a dense poorly altered and probably completely solidified intrusive body, located at ~1500 m depth.

The crustal seismic structure beneath Akutan and the neighboring Makushin Island was previously studied by Syracuse et al. (2014) by joint inversion of the body and surface wave data. In that study, the *P*-wave velocity was merely derived from the body waves, whereas the *S*-wave velocity was mostly obtained from using the surface-wave data. Therefore, the resolutions of the *P* and *S* wave models were incompatible that prevented obtaining robust values of the *Vp/Vs* ratio, which is an essential parameter for studying the presence of liquids and gases in the magmatic systems (e.g., Nakajima and Hasegawa, 2003; Chiarabba and Moretti, 2006; Koulakov et al., 2011; Vargas et al., 2017). Furthermore, the derived velocity models appeared to be too smooth: the presented results demonstrated general patterns for the entire Akutan-Makushin complex, but did not reveal details of the magmatic structures beneath each of these volcanoes.

Based on consideration of a series of previous tomography studies having similar distributions of stations and earthquakes (e.g., Koulakov et al., 2011; 2018; Kasatkina et al., 2014; Bushenkova et al., 2019), we propose that the available data in the case of Akutan may enable higher resolution than reported by Syracuse et al. (2014). The main purpose of this study is to revisit the updated Akutan seismological data and to obtain new details of the magmatic system beneath this volcano. Here, we especially focus on obtaining a reliable model of *Vp/Vs* ratio.

2. General information about Akutan

The volcanic activity beneath the Alaska and Aleutians is caused by the ongoing subduction of the Pacific Plate to the northwestern direction at a rate of ~68 mm/yr (e.g., Cross and Freymueller, 2008). The seismicity distributions in the Benioff zone shows that in the upper part, the slab subducts at an angle of 40°, while after reaching ~100 km depth, it steepens to ~60° (Jacob et al., 1977). The Akutan Island is located in the eastern side of the Aleutian Arc at the edge of the Alaskan shelf (Figure 1a), where the crust of the overriding plate is expected to be transitional from the continental to oceanic type. However, the results of receiver-function analysis (Janiszewski et al., 2013) report the crustal thickness of 33-39 km beneath Akutan, which is thicker than could be expected in such transitional settings. This could be explained by a stable location of the Aleutian subduction for millions years, leading to accumulation of considerable amount of volcanic material along several steady magma conduits (Myers et al., 1985).

The oldest formations of the Akutan Island are composed of Pliocene-Pleistocene volcanic rocks, dikes and sills mostly exposed in the eastern part of the island in the area of Hot Springs Bay Volcanics (HSBV) (Romick et al., 1990, McConnel et al., 1997). The ages of lava flows and pyroclastic deposits within these formations are estimated by Romick et al. (1990) at approximately 4 Ma. Almost everywhere on the island, the old structures are covered by younger (~ 1 Ma) lava flows of the Akutan volcanic (AKV) complex (Romick et al., 1990), which are probably related to the ancestral Akutan volcano edifice.

Most of the western part of the island is covered by Holocene lava flows and pyroclasts of the modern Akutan volcano (Figure 1b). Scoria and pumice bearing lapilli tephra, called the Akutan tephra, is widely presented as the youngest primary volcaniclastic deposits over the island area forming layers of about 2 m thick. It is interpreted as a result of a major caldera forming eruption of the Akutan volcano (Waythomas, 1999). Both old and recent volcanic rocks in Akutan demonstrate a broad variety of compositions ranged from magnesian basalts to dacites (45%-62% SiO_2) (Romick et al., 1990). The most primitive magnesian basalts are characteristic for the oldest HSBV, while the younger volcanics of AKV and modern Akutan volcano have more fractionated compositions.

The amount of hydrous phenocrysts suggests that more recent eruptions in the modern vent were fractioned at shallower magma levels compared to the older volcanic products in the eastern part of the island (Romick, 1990). Recent cones within the caldera and Holocene vents in the Lava Point area are dominated by porphyritic andesite with the contents of SiO_2 of 55-57.8% (Romick, 1990). However, lava flows and pyroclasts of historical eruptions are mostly represented by porphyritic basalts (Miller et al., 1998).

Fault structure of the Akutan Island, which is shown in Figure 1b, was studied in details within the scopes of the Akutan Geothermal Project (see Stelling et al., 2015 and references therein). The distributions of faults revealed the major NW/SE and E/W trending and generally dissect older geological formations of the island, but almost do not affect the modern Akutan volcano edifice.

Presently, the volcanic activity is mainly concentrated in areas of the Akutan stratovolcano and Lava Point in the western part of the island (Figure 1b). The volcano is headed by a circular caldera with the diameter of ~ 2 km having the highest point of the Akutan Peak at the altitude of 1303 m. In older literature sources, it was stated that the caldera was formed during an eruption 5200 years ago (Reeder, 1983, Miller et al., 1998). Later, based on studying tephra stratigraphy, Wathomas et al. (1999) argued that the caldera is significantly younger and might be originated during a large plinian eruption ~1600 years BP. In this case, the eruption 5200 years BP might be responsible for creating another larger caldera, whose traces are identified on the southern flank of the stratovolcano. Within the caldera, in its northwestern part, there is an active cone of 240 m high and ~1000 m wide, which is the main source of most recent lava flows. The permanent fumarole activity is observed on the southwestern flank of this cone. Inside the caldera, there are two lakes: a cold lake along the western wall and a small hot slightly acidic lake near the northern wall of caldera (Miller et al., 1998).

The recent episode of eruptive activity has probably begun between 9500 and 8500 years BP as recorded in pyroclastic sequences in the Western part of the island (Waythomas, 1999). Nowadays, Akutan is one of the most active volcanoes in the Aleutian Arc. Since 1790, at least 27 eruptions of Akutan were recorded (Simkin and Siebert 1994; Miller et al. 1998); however, the actual number could be much larger because many events remained undetected due to remoteness of the island and sparse population in the area. In twentieth century, Akutan demonstrated several small-to-moderate eruptions occurred from the intra-caldera cone. Three magmatic eruptions occurred in 1929, 1947-1948 and 1978 that produced lava flows of similar volumes and andesitic compositions that flowed from the caldera along the northern flank to a distance of approximately 700 meters. An eruption of Volcanic Explosivity Index VEI 2 occurred in 1948 and ejected an ash plume that reached the Akutan city located at ~13 km distance. The most recent eruptions of Akutan in 1983 and 1992 were characterized by strombolian activity and produced a series of steam emissions with a relatively small amount of ash plumes.

A remarkable seismic unrest in the area of the Akutan volcano occurred in 1996. The first seismic swarm stroke on March 11, 1996 and lasted for 11 hours. It included 80 earthquakes with magnitudes of more than M3.5 and a large amount of weaker events that were felt by inhabitants of the Akutan city almost continuously. The strongest event in this series reached the magnitude of M5.3 (Neal and McGimsey, 1997). Three days later, on 14 March, another swarm with 120 strong earthquakes lasted for 19 hours. The total energy released during these two swarms is compatible with that observed before the catastrophic eruption of Mount St. Helens in 1980 (Endo et al., 1981; Lu and Dzurisin, 2014**)** and is much larger than the energy of seismic precursors prior to the eruptions of Mt. Spurr in 1992 and Mt. Redoubt in Alaska in 1990 (Power et al., 1994, 1995; Lu and Dzurisin, 2014). The seismicity in the Akutan area was felt for several months and then gradually decayed without producing any volcanic eruption.

Immediately after beginning the unrest, the AVO scientists organized the deployment of seismic stations on the Akutan Island (Dixon et al., 2019). The first station started to operate in the city of Akutan on 12 March, just after terminating the first swarm. Later, on 18 March, four other stations were installed on the eastern part of the island. As there were no stations in the opposite side of the swarm, this first network only enabled very rough determinations of earthquake coordinates. Only in July 1996 a permanent network, which consisted of six telemetric stations, was installed on Akutan. Unfortunately, the locations of the strongest earthquakes, which stroke in the first days of the unrest in March 1996, remained unknown due to insufficient amount of stations. After installing the seismic network in July 1996, the swarm strongly decayed, but still hundreds of events were detected, most of which were located to the east of the Akutan stratovolcano in the upper part of the Hot Spring Valley.

During field works conducted in summer 1996, the AVO scientists discovered large ground fractures on the northwestern flank of the Akutan volcano between the caldera and Lava Point (Lu et al., 2000, 2005). The ground deformation zone was approximately 3 km long and 500 m wide (dashed line in Figure 1b) and included fractures with vertical displacements reaching 80 cm. Although no seismicity was detected in this zone during the March 1996 unrest, it is possible that the fist strongest seismic events with unknown coordinates stroke in this area and are responsible for forming these fractures. In July 1996, when the new network became capable to accurately localize the events, most of the seismicity was detected beneath the caldera area. Note that the maximum ground deformations in this area based on the SAR observations, were observed in the western part of the area [Lu and Dzurisin, 2014]. General uplift of up to 60 cm in a broad area on the western flank of Akutan coexisted with strong subsidence along the narrow fracture zone, which corresponds to the mechanism of a graben opening through a system of normal faults. Lu and Dzurisin [2014] estimated that these strong deformations were caused by a shallow intrusion at a depth of 0.5-2.5 km. In the eastern part of Akutan, ground deformations were identified along a 20 km long system of faults, where most of seismicity in the final stages of the unrest was recorded (Lu et al., 2005). At the same time, the measured deformations in the eastern part of the island were much weaker than those in the western part and reached the values of a few centimeters only. Lu and Dzurisin (2014) also presented surface deformations for seven years after this unrest and found that the general inflation continued, but with much smaller magnitude of less than 10 mm/year. They estimated that the source of this uplift was located at 5-6.5 km depth.

Another feature of seismic regime of Akutan is the existence of deep seismicity occurring in a broad range of depths in the middle and lower crust beneath the caldera area. Many of these events are identified as long-period earthquakes and interpreted as signatures of magma transport (e.g., Aki and Koyanagi, 1981). Note that similar deep crustal seismicity is observed beneath several other volcanoes, such as Aniakchak, Pavlof and Mount Spurr in Alaska [Power et al., 2004; Koulakov et al., 2013] and Klyuchevskoy in Kamchatka (Shapiro et al., 2017).

Akutan Island is an area of high geothermal activity. Within the caldera in the summit area of Akutan, several fumaroles on the active cone emit gases with the temperature of up to 96°C (Miller et al., 1998). The southern part of the caldera is covered by an acid lake with the temperature of up to 50°C. Besides the fumarole within the caldera, there is another fumarole field on the eastern flank of the volcano at an elevation of 350 m (Motyka et al., 1985; Stelling et al., 2015). This fumarole field consisting of steaming vents and boiling acid-sulfate springs has principally different physical and chemical properties compared to the main crater fumarole, which may indicate an existence of an impermeable barrier between them (Kolker et al., 2011). The flank fumarole field is located near the beginning of the Hot Spring Valley, which includes several groups of hot springs with temperatures of up to 94°C. Active hot springs also exist along the coast of the Hot Spring Bay, and they are strongly affected by tidal processes (Kolker et al., 2011). The magnetotelluric survey of this area has revealed a shallow low-resistivity layer representing horizontal aquifer connecting the flank fumarole and the hot spring areas (Mann et al., 2019).

3. Data and algorithm

In this study, we used arrival times of the *P* and *S* waves from local seismicity recorded by seismic stations installed on the Akutan Island. We use the data catalogue in the period of time from 1996 to 2017 generously provided to us by the AVO scientists. When selecting the data for tomography, we used three criteria: (1) The distance from an event to the nearest station should be less than 20 km; (2) the number of picks per event should be larger or equal 4; (3) the values of residuals after locating the sources in the starting 1D model should not be larger than 0.5 s. After applying these criteria, we selected 4,263 events with 19,081 *P*- and 22,901 *S*-wave picks (on average, 9.8 picks per event). The distributions of the relocated seismicity and seismic stations are presented in Figure 2. In two vertical sections, we present separately shallow seismicity (plots b and d) and the entire section down to 35 km including the deep seismicity (plots c and e). In the cases of b and d, we plot the events at distances of less than 2 km from the profile, whereas in c and e, the area of event selection is 8 km wide. It can be seen that most of the island area is covered by seismicity, which enables fair resolution of the tomography inversion.

To perform the tomographic inversion based on the local earthquake data, we use the LOTOS code (Koulakov, 2009), which was previously used for studying several volcanoes having similar geometry of stations and seismicity, such as Avacha volcano (Bushenkova et al., 2019) and Mount Spurr (Koulakov et al., 2013). As the input information, this code uses the arrival times of the *P* and *S* waves from seismic events located inside or slightly outside the recording network. The calculation procedure starts with determination of absolute coordinates of sources using the grid-search method. At this stage, the travel times between the sources and receivers are calculated along the straight lines, but using the 1D velocity model, which is an adequate approximation for small areas where the depths of events is compatible with the lateral size of the study area.

In the next step, we relocate the sources using a more accurate algorithm based on the bending method of the 3D ray tracing, which was initially proposed by Um and Thurber (1987). In the first iteration, the relocation is conducted in the starting 1D model, and in every new iteration, an updated 3D velocity model is used.

The three-dimensional velocity models are parameterized with a set of nodes distributed in the study volume according to the ray coverage. In map view, the nodes are regularly installed in areas with sufficient number of data (0.1 of average ray density) with the spacing of 1 km. In the vertical direction, the distance between nodes is inversely proportional to the ray density, but cannot be smaller than a predefined value (0.5 km in our case). Between the nodes, the velocity is approximated using the bi-linear interpolation. To reduce any dependency of the tomography results on the grid geometry, we performed a series of several inversions using several grids with different basic orientations of nodes. Then we calculate an average three-dimensional model in a regular grid, which is used for the relocation of sources in the next iteration. In total, we performed five iterations.

The inversion is performed using the LSQR algorithm (Paige and Saunders, 1982; Nolet, 1987) that allows fast solving linear equations with large and sparse matrices. The inversion is performed simultaneously for the *P* and *S* wave velocity models, source corrections (three coordinate and one time parameter) and station corrections (not used in our case). Furthermore, to control the stability of the inversion, we implement two types of damping. The amplitude of anomalies is controlled by additional trivial equations of $W^{am}dV_i=0$, where dV_i is velocity anomaly in the *i*-th node, and W^{am} is the coefficient of amplitude damping, which was equal to 0.2 and 0.4 for the *P* and *S* wave models respectively. The flatness of the retrieved anomalies was regularized by another set of equations: $W^{sm}(dV_k\text{-}dV_m) = 0$, where dV_k and dV_m are the velocity anomalies in the neighboring nodes *k* and *m*, W^{sm} is the flattening coefficient, which was equal to 0.6 and 1.2 for the *P* and *S* wave velocity models, respectively. The optimal values of the amplitude damping and flattening coefficients were determined using synthetic modeling.

4. Inversion results

The output of the tomography inversion includes the coordinates of relocated seismicity and three-dimensional distributions of the *P* and *S* velocities. Prior to discussing the main results of experimental data inversion, we present several synthetic test to demonstrate the resolution enabled by the existing data.

With synthetic tests, we tried to simulate the adequate conditions of data processing, same as exist in the case of experimental data inversion. The travel times were calculated in the 3D synthetic model for the same source-receiver pairs as in the original dataset using the 3D algorithm of ray tracing. Then the travel times were perturbed by random noise (0.05 s and 0.1 s for the *P* and *S* waves, respectively) that enabled the same variance reduction of the residuals during the inversion. Before starting the recovery of the model, we “forget” the true locations of the sources and start the workflow with absolute locations using the grid-search method, identically as we do for the experimental data. All the parameters and steps of the recovery procedure are the same as those used for computing the main model based on the experimental data. Same as in the case of experimental data inversion, in our tests, the *P* and *S* wave anomalies are calculated as independent parameters, and the *Vp/Vs* ratio is derived from a simple division of the absolute *P* and *S* wave velocities. In all cases, the results of synthetic modeling are shown for the *Vp/Vs* ratio, as this parameter appears to be most important for our interpretation.

In Figure 3, we present the checkerboard test aimed at assessing the horizontal resolution. In this case, we defined alternated anomalies of 3x3 km horizontal size separated from each other by 2 km wide areas without anomalies. The velocity anomalies in the synthetic model had the magnitudes of ±8% and they were opposite for the *P* and *S* anomalies that enabled strong variations of the *Vp/Vs* ratio. In this case, the anomalies remained unchanged with depth. The recovered distribution of the *Vp/Vs* ratio (calculated by division of the independently derived *P* and *S* wave velocities) shows fair resolution throughout the entire island area in sections at 1 and 4 km depth. In the deeper sections at 7 and 10 km depth, the anomalies are reconstructed only beneath the central and western parts of the island, where the middle and lower crust seismicity takes place. In the eastern part of the island, the anomalies are strongly smeared.

Figure 4 presents two other tests describing the cases when the velocity anomalies change their sign in the transition zone at depths 7-9 km. In the right column, the size of anomalies is the same as in the model presented in Figure 3 (3 km wide with 2 km of empty interval); whereas in the left column, the anomalies are larger: 4 km wide with 2 km of empty interval. It can be seen that the upper layer is recovered similarly as in the case when no depth change is defined. For the lower section, the recovering quality appears to be lower; however, most important anomalies are recovered at correct locations. Similarly as in Figure 3, the anomalies at 12 km depth are robustly recovered only in the central and western parts of the island.

To further assess the vertical resolution, we present another series of tests with anomalies defined along selected vertical sections. In this case, we used the anomalies of 4x4 km with empty intervals of 2 km. In the direction across the section, the anomalies were 10 km long. In Figure 5, we present four separate tests with models defined in each of four vertical sections used for presenting the main results. As in the previous cases, we present the recovered distributions of the *Vp/Vs* ratio. It can be seen that the tomography inversion resolves correctly the anomalies in the upper two rows. For the third row, the anomalies appear to be considerably smeared. Nevertheless, in all sections, the locations of the major structures are recovered at correct locations, although the amplitudes of the anomalies appear to be lower than in the original model. This should be taken into account when analyzing the results of experimental data inversion.

Another important test consists in inversions of two independent subsets separated by a random criterion, such as using events with odd or even numbers (odd/even test). All the processing stages and parameter values are identical to the case of the entire dataset inversion. This test is designed to assess the role of the random noise in the data to the inversion results. Indeed, in a case when the data are strongly perturbed by noise, the inversion results are strongly affected by random factors and in this case, the results of the odd/even test would be considerably different. If noise is not important in the data, the results appear to be similar. In this study, we present the inversion results for two datasets in two horizontal and three vertical sections. It can be seen that some minor details appear to be different; however, the major patterns that are important for our interpretation appear to be very similar, which shows that the random factor is not strong in this case.

The main result of this study is obtained after the tomographic inversion of experimental data includes the three-dimensional models of the *P* and *S* wave velocities (*Vp* and *Vs*), as well as the locations of more than 4000 seismic events used for tomography. The locations of the events are shown in map view and in two vertical sections in Figure 2. Instead of presenting absolute velocities, we prefer to show velocity anomalies relatively the starting model (*dVp* and *dVs*). We also show the distribution of the *Vp/Vs* ratio, which was obtained from a simple division of the absolute velocity values of *Vp* by *Vs*. As was demonstrated by synthetic tests, such scheme provides adequate recovery of the *Vp/Vs* ratio from independently derived *Vp* and *Vs*. The distributions of the *dVp*, *dVs* and *Vp/Vs* ratio are plotted in four horizontal sections in Figures 7 to 9 together with topography and major structural elements that are important for the interpretation. In these sections, areas with poorer resolution estimated from synthetic modeling are masked. The resulting models of *dVp*, *dVs* and *Vp/Vs* ratio are also presented in four vertical sections (Figures 10 to 12). These sections also include the final locations of seismic events located at distances of less than 0.5 km from the section.

The obtained three-dimensional velocity model is generally consistent with the tomography results derived by Syracuse et al. (2014). Similarly as in the previous study, the *P*-wave velocity anomalies presented in horizontal sections in Figure 7 demonstrate a high-velocity pattern beneath the western part of the island, which appears to be roughly centered with the Akutan caldera. At the same time, joint consideration of the *P* and *S* wave anomalies and the *Vp/Vs* ratio in our study gives some important details that were not observed previously. At 1 km and 4 km depth, the *dVp* and *dVs* structures generally match each other in shape, but different in amplitudes of heterogeneities. For example, a local low-velocity anomaly beneath the caldera at 4 km depth is very clear in *dVs*, and less prominent in *dVp*, which provides a high value of the

Vp/Vs ratio. Similar feature is observed at 1 km depth beneath the southeastern flank of the volcano: very low *dVs* and neutral *dVp* give high *Vp/Vs* ratio exceeding 2. Interpretation of these results will be given in the next section.

5. Discussion

The distributions of the *P* and *S* wave velocities, and especially that of the *Vp/Vs* ratio, can be used to reveal the geometry of the magma plumbing systems and to identify circulation paths of fluids beneath active volcanoes. In this chapter, we present the interpretation of the derived tomography model presented in Figures 7 to 12. Since the nature of seismic anomalies cannot always be derived unambiguously from seismic velocity parameters, in our discussion, we took into account all available information about Akutan from literature sources. In Figure 13, we present the resulting model that schematically demonstrates interactions of the main elements in the magma-fluid system beneath Akutan.

Magma sources beneath Akutan

In the lower part, the derived velocity model gives a clear image of a deep magma conduit beneath the Akutan Caldera. In Figures 7 to 8, at depths 7 and 10 km, the distributions of the *P* and *S* wave velocity anomalies look inversely correlated: the positive anomaly of *dVp* beneath the caldera coexists with the negative anomaly of *dVs*, which leads to elevated values of the *Vp/Vs* ratio indicated by "1" in Figures 9 and 12. As was shown by synthetic tests, we cannot ensure the correct amplitudes of anomalies at these depths; however, their locations and shapes are resolved correctly within the highlighted area. Such coexistence of higher *Vp* and lower *Vs* is a typical feature representing active magma conduits beneath many volcanoes of the world. The most similar case is Mount Spurr, for which the tomography study by Koulakov et al. (2013) has revealed almost identical columnar structure of high *Vp/Vs* ratio. The other cases of coexistence of high *Vp*, low *Vs* and high *Vp/Vs* beneath active volcanoes are: Colima Volcanic Complex (Sychev et al., 2019), Avacha Volcano Group (Bushenkova et al., 2019), Gorely (Kuznetsov et al., 2017), Nevado del Ruiz (Vargas et al., 2017) and many others.

This inverse correlation follows from fundamentally different sensitivity of the *P* and *S* waves to the physical properties of rocks (Takei, 2002; Koulakov et al., 2013). Indeed, the *P*-wave velocity is more sensitive to the composition and is usually higher for magmas ascending from deeper sources having more primitive compositions with respect to surrounding rocks. At the same time, the *S*-wave velocity is sensitive to the presence of liquid phases and is usually low in partially molten magmas with high content of dissolved volatiles. That is why, the coexistence of high *Vp*, low *Vs* and very high *Vp/Vs* ratio in columnar anomalies beneath active volcanoes is usually interpreted as a conduit area delivering magmas with high contents of melts and/or dissolved volatiles, which is applicable to the case of Akutan. In vertical sections in Figures 10 to 12, we can see that the top of such columnar conduit ("1") may be located at a depth of ~5-6 km below surface. This appears to be consistent with the modeling of SAR deformations by Lu and Dzurisin (2014), in which the upper limit of a body responsible for the inflation in 1997-2012 was estimated at this depth.

In the shallower layers above 5 km below surface, the structure of seismic velocities appears to be more complicated than in the lower part of the model. We propose that the seismic heterogeneities at these depths are mostly controlled by a complex interaction of fluid flows and magma bodies, as schematically shown in Figure 13. In section at 1 km b.s.l. (Figure 9), the most prominent feature is a series of WNW-ESE oriented anomalies of high *Vp/Vs* ratio. We propose that these anomalies may represent a chain of shallow magma reservoirs associated to the mechanically weak segment of fractured zone crossing the island and having the same dominant orientations of faults (Figure 1b).

In map view at 1 km depth in Figure 9, we observe a prominent anomaly of high *Vp/Vs* ratio beneath the southeastern rim of the caldera marked by "2". In vertical section 1 (Figure 12), we see that this anomaly has an inclined shape and appears to the surface on the southeastern flank of the volcano. We propose that this anomaly, at least its lower part located at depths 2-4 km b.s.l., represents a magma reservoir that possibly acts as a main source delivering the magmatic material to recent summit eruptions of Akutan. At the same time, the uppermost part of this anomaly reaching the surface at the southeastern flank of the volcano may represent the down-going flow of meteoric fluids. The processes of partial melting and fluid saturation have similar signatures in the *Vp/Vs* ratio distribution; therefore, in our tomography images, we cannot identify which of these two factors is responsible for originating this anomaly. If they both act in this case, merely from the *Vp/Vs* model, we cannot resolve a boundary between the magma reservoir and host rocks soaked by meteoric fluids. At the same time, we see that the deepest part of this anomaly is associated with strong seismicity that may reflect active processes of degassing, phase transitions and magma movement causing abrupt changes in stress regime in the magma feeding system. Therefore, we may roughly define the aseismic shallow part of the anomaly "2" down to the depth of ~1 km as an area affected by the meteoric fluid flow, and the seismically active deeper part of this anomaly as a magma reservoir (Section 1, Figure 12). In vertical sections 1, 2 and 3 (Figures 12 and 13), the anomaly “2” appears to be connected with the deep conduit “1”. The fact that the shallow magma reservoir is located right above the deep conduit and appears to be directly connected with it may explain the long-term volcanic activity of the Akutan volcano at a steady location.

To the east from the modern volcano edifice, in horizontal section at 1 km depth (Figure 9), we observe a large shallow anomaly of high *Vp/Vs* ratio marked by “3”. In vertical section 2 (Figure 12), this anomaly is traced down to the depth of ~3 km below surface and appears to be connected with anomaly “2” at the vicinity of the caldera. Although there is no any manifestation of volcanic or geothermal activity on the surface above the anomaly “3”, we propose that it may represent a “dormant” magma reservoir that was formed in this zone weakened by tectonic faulting. This hypothesis is supported by the occurrence of a large number of seismic events and strong ground deformations during the unrest in 1996-1998 at the locations coinciding with this anomaly (Lu et al., 2000; Siracuse et al., 2014), which may indicate an episodic activation of this magma reservoir. Alternatively, one may explain this and other shallow anomalies of high *Vp/Vs* ratio beneath Akutan by saturation of rocks by meteoric fluids. This might be partly true, at least for the uppermost part, as this anomaly is located in a highly dissected fractured zone having higher permeability. At the same time, we find it unlikely that meteoric water may penetrate down to the depth ~3 km below surface, at which the anomaly is observed. If we assume that the anomaly “3” (or at least its deeper part) represents a shallow magma reservoir, it might be fed by lateral magma migration from the anomaly “2”. Alternatively, the magma can be delivered directly from the deep conduit, as schematically shown in Figure 13, through the system of dykes and sills that remains hardly resolvable for our tomography inversion.

Another shallow high *Vp/Vs* anomaly marked by “4” is observed beneath the western flank of the Akutan volcano. This anomaly is located at a distance of 2-3 km to the south of the Lava Point, where lava flows and scoria cones were produced by the 1948 eruption. It cannot be excluded that this area of high *Vp/Vs* ratio represents a magma storage that fed the eruptions of Lava Point. This anomaly might also be associated with strong ground deformations taken place during the seismic crisis in March 1996, which caused the origin of fractures on the surface with the vertical displacements reaching 80 cm. This scenario will be discussed in more details later in this paper.

Fluid migration in geothermal system of Akutan

The Akutan Island hosts several sites of elevated geothermal activity including two distinct fumarole fields: one is on the active cone inside the caldera (Summit Fumarole – SF) and another one is on the eastern flank of the volcano at the altitude of 350 m a.s.l. (Flank Fumarole – FF). A model describing the origin of geothermal activity in Akutan was developed by Kolker et al. (2011) and then substantiated by more detailed geochemical, geological and geophysical surveys in (Bergfeld et al., 2014; Stelling et al., 2015). This model presumes two separate hydrothermal systems: one is connected to SF on the intracaldera cone of the Akutan volcano, and another is responsible for feeding FF and thermal sources in the Hot Spring Bay Valley (HSBV). Different geochemical fingerprints of SF and FF products imply that they are fed from separate hydrothermal resources. Comparison of gas compositions shows that both fumarole fields contain gases from juvenile magmatic sources, but SF gases are more contaminated by cold meteoric waters, while in FF this contamination is less pronounced (Bergfeld et al., 2014). This concept seems to be supported by our results. The distribution of the *Vp/Vs* ratio in section 3 (Figure 12) shows that at a depth of ~4 km b.s.l., the deep magma conduit is split in two branches under the locations of SF and FF. Beneath SF, the branch evolves into a prominent anomaly of high *Vp/Vs* ratio representing a shallow reservoir with partially molten magma. Beneath FF, the anomaly is less prominent and even evolves to low *Vp/Vs*. In some previous tomography studies of volcanoes with high level of gas emission, the anomalies of low-Vp/Vs ratio were interpreted as gas-contaminated areas (Husen et al., 2004; Koulakov et al., 2013, 2018, Kuznetsov et al., 2017). Indeed, porous rocks filled with gas behave as a sponge with very low bulk elastic properties (low *Vp*), but normal shear strength (neutral *Vs*) that leads to low values of the *Vp/Vs* ratio (Takei, 2002). Based on this feature and the observed *Vp/Vs* distributions, we can propose that beneath SF, the medium is mostly saturated with liquid phases (melts), whereas beneath FF, the gaseous phase dominates. This explains a larger amount of juvenile gases in FF compared to SF.

The tomography model gives a possibility to trace the pathways of meteoric fluids in the uppermost layers of the crust. We distinguish several areas with very high *Vp/Vs* ratio reaching the surface. One of such anomalies outcrops in the western side of the island and is clearly seen as an inclined anomaly of high *Vp/Vs* ratio in the left side of Section 3 in Figure 12. Another one is observed on the southeastern flank of the modern Akutan volcano just below the rim of the caldera (an inclined anomaly in the summit area in Sections 1 and 4 in Figure 12). The third anomaly outlines bottoms of circular valleys presumably of glacial origin in the eastern part of the island (an anomaly in the right side of Section 2 in Figure 12). All the reported areas lack of any manifestations of ongoing magmatic activity, thus the only explanation for these anomalies might be saturation with groundwaters, which can percolate down to expected local aquifers. These and other possible areas of meteoric water penetration are schematically indicated in Figure 13 by dotted green arrows. It is seen that they may contribute to feeding the both SF and FF, as well as hot springs in HSBV.

The conceptual model of the hydrothermal flow in FF and HSBV implies concurrent up- and outflow of fluids from the same hydrothermal resource schematically indicated in Figure 13 as a blue reservoir beneath FF. The upflow at FF brings to the surface the gases enriched in juvenile components. The intake of gases from the magma reservoir to surface is confirmed by the high Cl-/F- ratio in hot springs (Bergfeld et al., 2013). Earlier studies (Giggenbach, 1996; Shinohara et al., 2008) have shown that the Cl-rich composition of volcanic gases suggests magma degassing. High concentrations of Cl- in thermal spring discharges can be attributed to an input of magmatic gases from a shallow magma chamber.

The outflow is composed of a large amount of degassed hydrothermal fluids trapped by reduced clay cap, which directs the flow horizontally to the east and then to northeast down to the hot springs of HSBV after significant mixing with the meteoric waters (Stelling et al., 2015 and references therein). This lateral flow is schematically indicated in Figure 13 as a blue layer and an arrow between FF and HSBV. According to MT survey, the HSBV hydrothermal fluids originate in a reservoir beneath FF consisting of intermediate resistivity rocks (50 – 100 Ohm m), extending down to the depth of 1500 m b.s.l., and rooted by a high-resistivity body. The latter is supposed to be a magmatic intrusion providing both heat and juvenile fluids (Ohren, 2013; Stelling et al., 2015), which is revealed in our model as an anomaly of high *Vp/Vs* beneath FF in Section 2 (Figure 13). However, there are some differences in imaging of this body by MT and seismic tomography. In the seismic model, the outline of this anomaly tops at ~ 2.5 km b.s.l., which differs from 1.5 km b.s.l., determined on the basis of MT survey data. One of explanations could be that the recorded anomaly represents the portions of cooling magma reservoir with minor residual melt, while swarm of surrounding dikes that propagated up to the 1.5 km b.s.l. already lack magmatic liquids, but still are pathways for magmatic gas and heat. These solidified upper parts of magmatic body could be associated with hydrothermally altered wallrocks, containing quartz, chalcedony and anhydrite similarly to inactive ancient hydrothermal system confined to the Long Valley extrusions and breccia (Figure 1). Hydrothermal mineralization blocks porosity of initial rocks and increases local resistivity.

For the area of HSBV and FF, the magnetotelluric (MT) measurements (Ohren et al., 2013; Mann et al., 2019) identified a low-resistivity shallow layer of 200-400 m thick underlain by high-resistivity material of unknown thickness. This shallow layer was interpreted as a permeable aquifer that delivers hot water from the area of FF to the hot springs. In a seismic velocity model, this layer would be expressed as an anomaly of high *Vp/Vs*, but, unfortunately, in our case, it appears too thin to be resolved by the local earthquake tomography. In our results, beneath HSV, we observe a prominent low-*Vp/Vs* ratio (less than 1.5). Such low *Vp/Vs* ratio could be interpreted as a signature of gas contamination, as was observed in some previous tomography studies of volcanoes with high level of gas emission (Husen et al., 2004; Koulakov et al., 2013, 2018, Kuznetsov et al., 2017). At the same time, in the geothermal sources of HSBV there are no evidences of gases coming from deeper layers. Furthermore, the hypothesis of gas contamination is not supported by the results of drilling of boreholes in HSBV (Mann et al., 2019). Two of them reached the depths of 450 and 600 meters, where the temperature was 160-170°C, which was still below boiling temperatures affected by lithostatic pressure, and no traces of steam were detected at these depths.

Another cause for the low *Vp/Vs* ratio was proposed by Lin and Shearer (2009) for the case of the San-Andreas fault. They claimed that a special shape of cracks filled with water may also lead to considerable decrease of *Vp/Vs*. In their model, they obtained low values of *Vp/Vs* ratio for rocks with the aspect ratio of the cracks (ratio of the minimum to maximum size) larger than 0.1 and the porosity of several percent. A medium with isometrical pores can be easily produced in volcanic rocks and might appear to be a plausible explanation for the observed low values of the *Vp/Vs* ratio beneath HSBV. However, in this case, the water-saturated porous medium would be electrically conductive, which would contradict the existing MT observations revealing high-resistivity in deep layers beneath HSBV. The low *Vp/Vs* also exists in rocks with anomalously high quartz content, such as quartz-rich gneisses and schists (Christensen, 1996; McCaffree and Christensen, 1998). In this case, we can achieve low *Vp/Vs* ratio without requesting high porosity in rocks, which would provide low resistivity observed in the MT studies. In any case, we do not have yet sufficient data to give a definitive answer about the nature of this low *Vp/Vs* anomaly, which requires further investigations in this area.

Causes of the 1996 seismic unrest

As was described earlier, a strong seismic crisis started in the Akutan Island in March 1996 and lasted for several months without producing any volcanic activity. Such “missed” eruption is a quite frequent phenomenon that is observed in some active and dormant volcanoes of the

World. For example, in late 2017, a strong seismic swarm started beneath the Udina volcano in Kamchatka, which was earlier considered as extinct. Deploying a temporary seismic network has proven the active state of the magma system beneath this volcano (Koulakov et al., 2019). However, the seismic unrest, which started on December 2017 and continued until now, did not lead to any manifestations of volcanic activity. A similar seismic swarm took place in the area of Asacha, which is another extinct volcano in Kamchatka (Tokarev, 1984). Nearly 1000 seismic events stroke in 1983, some of which were felt by workers in a mining settlement at the vicinity of the volcano and caused serious damages in buildings. However, this swarm gradually ceased without producing any volcanic activity of Asacha.

Another case of "missed" eruption occurred in Harrat Lunayyir in April-June 2009, which is an area of intracontinental basaltic volcanism in Saudi Arabia (Pallister et al., 2010). More than 30,000 events were recorded, of which dozens had magnitudes higher than Mw 4, and the strongest event reached the magnitude of Mw 5.4. Similarly, as in the case of Akutan, this seismic unrest caused considerable ground deformations measured by InSAR (Baer and Hamiel, 2010) and led to forming a system of fractures on the surface. The causes of this unrest in Harrat Lunayyir were investigated using seismic tomography studies. Based on the travel time tomography, Koulakov et al. (2015) revealed an anomalous body with high Vp/Vs ratio, which was interpreted as a magma reservoir. In shallow layers, the anomaly of low Vp/Vs ratio was interpreted as an impermeable rigid basaltic cover that prevented magma intrusion to the surface. In the later study by Sychev et al. (2017), seismic attenuation tomography has identified a shallow high attenuation zone coinciding with maximum ground deformation that was interpreted as a conduit for gases escaping from the magma reservoir.

The final example, which appears to be most similar to the case of Akutan, is the unrest of Mount Spurr in 2004-2006. Recent explosive eruptions of Mount Spurr, such as ones of 1953 and 1992, occurred through the flank Crater Peak, but the summit area was considered as inactive for more than 5,000 years. In 2004-2005 unusually strong seismic swarm beneath the summit area was accompanied by inflation of up to 10 cm (Lu and Dzurisin, 2014), as well as by activation of thermal processes and gas flux in the summit crater. Similarly to the case of Akutan, deep seismicity in the middle and lower crust marked the location of the magma conduit, which was clearly revealed by seismic tomography as a columnar anomaly of high *Vp/Vs* (Koulakov et al., 2013). Time-dependent tomography study by Koulakov et al. (2018) has demonstrated that during the seismic unrest in 2004-2006, the upper boundary of this conduit-related anomaly shifted upward from the depth of ~5 km to ~3 km below surface. Koulakov et al. (2018) proposed a scenario that led to the seismic and geothermal activity in Mount Spurr in

2004-2006, which was based on the concept established by Fournier (1999) and Mercier and Lowell (2016). The magma reservoir at ~5 km was a ductile body surrounded by a rigid self-sealed zone (SSZ), which remained impermeable most of time. Gradual income of fluids from deeper sources led to reaching a critical concentration of volatiles in the upper part of the reservoir. At some moment, they broke the SSZ and entered to the brittle zone of the upper crust. Over-pressurized fluids easily created cracks and ascended toward the surface. At some depth, decompression caused separation of supercritical fluids into liquid and gas that led to additional stresses and triggered seismicity. The apparent uplift of the upper limit of the *Vp/Vs* anomaly during the unrest period was associated with fast migration of fluids from the ductile reservoir through the brittle cover. The boundary between the high and low *Vp/Vs* ratio at ~3 km depth represented the level of phase separation of escaping juvenile fluids.

We propose that similar processes as described in the previous paragraph for the Mount Spurr might take place during the seismic unrest in Akutan in 1996. Unfortunately, there was not a sufficient seismic network in that time to build the geometry of the feeding system during the unrest, as was done for the cases of Harrat Lunayyir and Mount Spurr. We confess that the present seismic structure based on the long-term observations from 1996 to 2017 may be significantly different of that existed in the moment of crisis. Nevertheless, we propose that some structural elements revealed now can help us to identify the mechanism of the unrest of Akutan in 1996.

The main deformations on the surface took place in the western part of the island between the Akutan summit and Lava Point. The deep structure beneath this segment can be observed in the left side of Section 2. We see that the top of the magma conduit associated with the anomaly of high *Vp/Vs* ratio is located at a depth of 5-6 km below surface. Above this anomaly, we observe some local patterns with high Vp/Vs ratio, which possibly mark the ascent of magma fluids. Just below the western flank of Akutan, we observe a shallow anomaly of low *Vp/Vs* ratio. This looks similar to the case of Harrat Lunayyir (Koulakov et al., 2015), where strong surface deformations occurred in a zone with shallow anomalies of low *Vp/Vs* ratio. Based on only seismic velocities, we cannot recognize if this feature corresponds to a rigid cover or is caused by presence of gas contaminated fractures or conduits in this massif. Unfortunately, the information on attenuation, which appeared very efficient for the case of Harrat Lunayyir to distinguish these factors, is not yet available for Akutan.

Based on the obtained tomography model of Akutan and the existing tomography results for Harrat Lunayyir and Mount Spurr that experienced similar seismic unrests, we propose a scenario explaining a strong seismic swarm in Akutan in 1996. We think that the deep columnar anomaly of high Vp/Vs ratio beneath the Akutan caldera represents a steady magma conduit that exists here for long time of the development of the island. This conduit consists of ductile rocks with high content of melt. In normal state, this conduit is covered by a low-permeable rigid self-sealed zone that prevents escaping fluids from the conduit. However, with time, the amount of fluids gradually increased, and in some moment, they reached a critical concentration and destroyed the rigid cover. Otherwise the fluids could escape due to tectonic movements and mechanical weakening of the SSZ. After that, the juvenile fluids appeared in the brittle upper part of the crust and quickly created a system of cracks enabling fast migration of the fluids to the surface. At some depth, the magmatic fluids were separated into liquid and gas, which led to an avalanche-type expansion in the uppermost layers and caused fracturing and deformations observed on the surface. After releasing the excessive fluids form the magma conduit, their flow stopped, and the seismic process gradually ceased.

According to this scenario, such unrests are not associated with any magma movement in the reservoir and merely triggered by fluid migration and phase transformations. Nevertheless, the associated fracturing may weaken the rigid cover and create a pathway for a future magmatic eruption.

Conclusions

In this study, we have presented a seismic model (*Vp*, *Vs* and *Vp/Vs* ratio) of the Akutan volcanic island in the eastern part of the Aleutian Arc based on tomographic inversion of a dataset including arrival times of the *P* and *S* seismic waves from more than 4000 local events. The reliability and spatial resolution of this model was carefully verified using a set of different tests. The obtained seismic structures shed light to the details of functioning the magma plumbing system and its interaction with the fluid dynamics in the crust beneath areas of fumarolic and geothermal activity.

Below 5 km depth, beneath the caldera and the presently active volcanic cone, we observe a prominent anomaly of high *Vp*, low *Vs* and high *Vp/Vs* ratio coinciding with the locations of deep seismicity that occurs throughout the crust down to ~35 km depth. We interpret this anomaly as a steady deep magma conduit that controls the volcanic activity of Akutan.

At shallower layers, the seismic structures appear to be more complicated and likely associated to an interaction between magma reservoirs and fluid circulations. Beneath the main active cone within the caldera, we observe a contrasted shallow anomaly of high *Vp/Vs* representing a shallow magma reservoir, which is directly responsible for feeding the recent eruptions of Akutan. Beneath the eastern flank of the volcano, we observe a large elongated anomaly of high *Vp/Vs* ratio reaching the depth of ~3 km. We interpret it as another shallow magma reservoir formed in a weakened fracture zone crossing the island in the WNW-ESE direction. The active state of this magma body is evidenced by considerable ground deformations and seismicity occurred in 1996-1998.

Our tomography model shed light to the cause of distinct behavior of the Summit and Flank Fumarole fields (SF and FF), having considerably different signatures of juvenile fluids. We see that at ~4 km depth, the deep magma conduit is split in two isolated branches following to SF and FF. The SF branch evolves into a contrasted anomaly of high Vp/Vs ratio representing the shallow magma reservoir, in which the liquid phases (melts) are dominating. Another branch appears to be less prominent and possibly represent a pathway of the degassed juvenile fluids towards FF. Mixing these fluids with meteoric water gives the origin for a lateral flow toward the Hot Spring Bay Valley, where a series of geothermal springs and pools are observed. We also observe several prominent anomalies at the surface in different parts of the Akutan Island that are interpreted as zones of active penetration of meteoric water to the ground.

Based on consideration of our tomography model and taking into account similar cases of Mount Spurr in 2004-2009 and Harrat Lunayyir in 2009, we propose a scenario of magma-fluid interaction that led to the strong seismic unrest of Akutan in 1996. We hypothesize that strong seismic swarm occurred due to abrupt injection of magmatic fluids from ductile magma conduits to brittle crustal cover. Fast migration of fluids along hydro-fractures and avalanche-type degassing due to decompression led to a series of high-magnitude earthquakes and considerable surface deformations in the western part of the island. Thus, we conclude that the 1996 unrest was mainly triggered by the fluid migrations and phase transitions and did not involve any magmatic activity. At the same time, we cannot exclude that the associated fracturing might weaken the rigid cover and create a pathway for a future magmatic eruption.

Acknowledgments:

We thank Jim Dixon from AVO who provided us the data for this study. This study was supported by the Russian Science Foundation Grant # 20-17-00075. SZS is supported by the Integration Project of SB RAS #44.

Derived products from this publication, including travel times of P and S waves and the full folder of the LOTOS code that allows reproducing all the results of this research are presented in the file depositary: Koulakov Ivan. (2020). LOTOS coce of local earthquake tomography with the Akutan dataset [Data set]. Journal of Geophysical Research, Solid Earth. Zenodo. http://doi.org/10.5281/zenodo.3946666

The authors declare no financial conflicts of interest.

Figure captions:

Figure 1. Study area. a. General view to the eastern part of the Aleutian arc and Alaska. Background is the shaded topography. Red dots are the Holocene volcanoes. Dotted lines indicate the dipping of the slab with the interval of 50 km. b. Topography and generalized geology of the Akutan Island by (Richter et al., 1998) with modifications: 1 - modern Akutan volcano with its lava flows and pyroclastic deposits; 2 - older subsidiary vents with lava plugs and breccia (a) and lava flows (b); 3 - caldera rims; 4 - scoria cones; 5 - flank fumarole field (a) and Hot Springs Bay Valley hot springs (b) ; 6 - active thermal spring and fumarole area (Ohren et al., 2013); 7 - inactive hydrothermal activity area (Mann, 2019); 8 - faults (Stelling et al., 2015).

Figure 2. Locations of seismicity in map view (upper plot) and in two vertical sections. In map view, the colored dots represent the events classed by depth. Red triangles depict the seismic stations used in this study. For each vertical section, we present events in a shallower part (left row) and in a larger area (right row). Maximum distances from the events to the profile are indicated in captions at each plot.

Figure 3. Checkerboard for testing the horizontal resolution, in which the synthetic anomalies do not change with depth. The dotted lines highlight the locations of the synthetic anomalies. Here, we show only the recovered distributions of the Vp/Vs ratio. Contour lines depict the topography with the interval of 200 m. The areas with poorer resolution are masked.

Figure 4. Checkerboard for testing the horizontal and vertical resolution. In this case, the sign of the synthetic anomalies changes in the depth interval from 6 to 8 km. The dotted lines

highlight the locations of the synthetic anomalies. Here, we show only the recovered distributions of the Vp/Vs ratio. Contour lines depict the topography with the interval of 200 m. The areas with poorer resolution are masked.

Figure 5. Synthetic tests for checking the vertical resolution. Each plot represents a separate model defined along one of four vertical sections. The recovered results are shown for the Vp/Vs ratio.

Figure 6. Odd/even test consisting in independent inversions of two subsets separated by a random criterion (with odd and even numbers of events). The resulting distributions of the Vp/Vs ratio are shown in two horizontal sections and three vertical sections.

Figure 7. P-wave velocity anomalies derived from the inversion of experimental data presented in four horizontal sections.

Figure 8. S-wave velocity anomalies derived from the inversion of experimental data presented in four horizontal sections.

Figure 9. Vp/Vs ratio derived from the inversion of experimental data presented in four horizontal sections.

Figure 10. P-wave velocity anomalies derived from the inversion of experimental data presented in four vertical sections whose locations are indicated in Figures 7 to 9. Dots indicate the locations of the events at distances less than 1 km from the profile.

Figure 11. S-wave velocity anomalies derived from the inversion of experimental data presented in four vertical sections whose locations are indicated in Figures 7 to 9. Dots indicate the locations of the events at distances less than 1 km from the profile.

Figure 12. Vp/Vs ratio derived from the inversion of experimental data presented in four vertical sections whose locations are indicated in Figures 7 to 9. Dots indicate the locations of the events at distances less than 1 km from the profile.

Figure 13. Schematic interpretation of the resulting distributions of the Vp/Vs ratio in vertical sections 2A-2B and 3A-3B, same as shown in Figure 12. See details in the text.

References

Aki, K., & Koyanagi, R. (1981). Deep volcanic tremor and magma ascent mechanism under Kilauea, Hawaii. *Journal of Geophysical Research*, *86*(B8), 7095–7109. https://doi.org/10.1029/JB086iB08p07095

Baer, G., & Hamiel, Y. (2010). Form and growth of an embryonic continental rift: InSAR observations and modelling of the 2009 western Arabia rifting episode. *Geophysical Journal International*, *182*(1), 155–167.

Benz, H. M., Chouet, B. A., Dawson, P. B., Lahr, J. C., Page, R. A., & Hole, J. A. (1996). Three-dimensional P and S wave velocity structure of Redoubt Volcano, Alaska . *Journal of Geophysical Research: Solid Earth*, *101*(B4), 8111–8128. https://doi.org/10.1029/95jb03046

Bergfeld, D., Lewicki, J.L., Evans, W.C., Hunt, A.G., Revesz, K., & Huebner, M. (2013). *Geochemical investigation of the hydrothermal system on Akutan Island, Alaska, July 2012*. Scientific Investigations Report 2013–5231. https://doi.org/http://dx.doi.org/10.3133/

Bushenkova, N., Koulakov, I., Senyukov, S., Gordeev, E. I., Huang, H. H., El Khrepy, S., & Al Arifi, N. (2019). Tomographic Images of Magma Chambers Beneath the Avacha and Koryaksky Volcanoes in Kamchatka. *Journal of Geophysical Research: Solid Earth*, *124*(9), 9694–9713. https://doi.org/10.1029/2019JB017952

Casadevall, T. J. (1993). Volcanic hazards and aviation safety. Lessons from the past decade. *Flight Safety Foundation–Flight Safety Digest*, 1–9.

Chiarabba, C., & Moretti, M. (2006). An insight into the unrest phenomena at the Campi Flegrei caldera from Vp and Vp/Vs tomography. *Terra Nova*, *18*(6), 373–379. https://doi.org/10.1111/j.1365-3121.2006.00701.x

Christensen, N. I. (1996). Poisson's ratio and crustal seismology. *Journal of Geophysical Research B: Solid Earth*, *101*(2), 3139–3156. https://doi.org/10.1029/95jb03446

Cross, R. S., & Freymueller, J. T. (2008). Evidence for and implications of a Bering plate based on geodetic measurements from the Aleutians and western Alaska. *Journal of Geophysical Research: Solid Earth*, *113*(7), 1–19. https://doi.org/10.1029/2007JB005136

Dixon, J. P., Stihler, S. D., Haney, M. M., Lyons, J. J., Ketner, D. M., Mulliken, K. M., Parker, T., & Power, J. A. (2019). *Catalog of earthquake parameters and description of seismograph and infrasound stations at Alaskan volcanoes—January 1, 2013, through December 31, 2017*. US Geological Survey.

Endo, E.T., Malone, S.D., Noson, L.L., & Weaver, C. S. (1981). Locations, magnitudes and statistics of the March 20 - May 18 earthquake sequence. In U. S. Lipman, P.W. and Mullineaus, D.R. (Ed.), *The 1980 Eruptions of Mount St. Helens, Washington* (Geological, pp. 93–107).

Fournier, R. O. (1999). Hydrothermal processes related to movement of fluid from plastic into brittle rock in the magmatic-epithermal environment. *Economic Geology*, *94*(8), 1193–1211. https://doi.org/10.2113/gsecongeo.94.8.1193

Giggenbach, W. F. (1996). Chemical Composition of Volcanic Gases. In *Monitoring and Mitigation of Volcano Hazards* (Vol. 24, pp. 221–256). Berlin, Heidelberg: Springer Berlin Heidelberg. https://doi.org/10.1007/978-3-642-80087-0_7

Husen, S., Smith, R. B., & Waite, G. P. (2004). Evidence for gas and magmatic sources beneath the Yellowstone volcanic field from seismic tomographic imaging. *Journal of Volcanology and Geothermal Research*, *131*(3–4), 397–410. https://doi.org/10.1016/S0377-0273(03)00416-5

Jacob, F. (1977). Evolution and tinkering. *Science*, 196(4295), 1161-1166.

Janiszewski, H. A., Abers, G. A., Shillington, D. J., & Calkins, J. A. (2013). Crustal structure along the Aleutian island arc: New insights from receiver functions constrained by active-source data. *Geochemistry, Geophysics, Geosystems*, *14*(8), 2977–2992. https://doi.org/10.1002/ggge.20211

Kasatkina, E., Koulakov, I., West, M., & Izbekov, P. (2014). Seismic structure changes beneath Redoubt Volcano during the 2009 eruption inferred from local earthquake tomography. *Journal of Geophysical Research: Solid Earth*, *119*(6), 4938–4954. https://doi.org/10.1002/2013JB010935

Kolker, A., Cumming, W., Stelling, P., Prakash, A., & Kleinholz, C. (2011). *Akutan geothermal project*. *In Renewable Energy Alaska Project (REAP) Forum*.

Koulakov, I., Smirnov, S. Z., Gladkov, V., Kasatkina, E., West, M., El Khrepy, S., & Al-Arifi, N. (2018). Causes of volcanic unrest at Mt. Spurr in 2004–2005 inferred from repeated tomography. *Scientific Reports*, *8*(1), 1–7. https://doi.org/10.1038/s41598-018-35453-w

Koulakov, I. (2009). LOTOS code for local earthquake tomographic inversion: Benchmarks for testing tomographic algorithms. *Bulletin of the Seismological Society of America*, *99*(1), 194–214. https://doi.org/10.1785/0120080013

Koulakov, I., Gordeev, E. I., Dobretsov, N. L., Vernikovsky, V. A., Senyukov, S., & Jakovlev, A. (2011). Feeding volcanoes of the Kluchevskoy group from the results of local earthquake tomography. *Geophysical Research Letters*, *38*(9), 1–6. https://doi.org/10.1029/2011GL046957

Koulakov, I., West, M., & Izbekov, P. (2013). Fluid ascent during the 2004-2005 unrest at Mt. Spurr inferred from seismic tomography. *Geophysical Research Letters*, *40*(17), 4579–4582. https://doi.org/10.1002/grl.50674

Koulakov, I., Khrepy, S. El, Al-Arifi, N., Kuznetsov, P., & Kasatkina, E. (2015). Structural cause of a missed eruption in the Harrat Lunayyir basaltic field (Saudi Arabia) in 2009. *Geology*, *43*(5), 395–398. https://doi.org/10.1130/G36271.1

Koulakov, I., Komzeleva, V., Abkadyrov, I., Kugaenko, Y., El Khrepy, S., & Al Arifi, N. (2019). Unrest of the Udina volcano in Kamchatka inferred from the analysis of seismicity and seismic tomography. *Journal of Volcanology and Geothermal Research*, *379*, 45–59. https://doi.org/10.1016/j.jvolgeores.2019.05.006

Koulakov, I., Boychenko, E., & Smirnov, S. Z. (2020). Magma chambers and meteoric fluid flows beneath the atka volcanic complex (Aleutian islands) inferred from local earthquake tomography. *Geosciences (Switzerland)*, *10*(6), 1–18. https://doi.org/10.3390/geosciences10060214

Kuznetsov, P. Y., Koulakov, I., Jakovlev, A., Abkadyrov, I., Deev, E., Gordeev, E. I., et al. (2017). Structure of volatile conduits beneath gorely volcano (Kamchatka) revealed by local earthquake tomography. *Geosciences (Switzerland)*, *7*(4), 3–7. https://doi.org/10.3390/geosciences7040111

Lin, G., & Shearer, P. M. (2009). Evidence for water-filled cracks in earthquake source regions. *Geophysical Research Letters*, *36*(17), 1–5. https://doi.org/10.1029/2009GL039098

Lu, Z., & Dzurisin, D. (2014). *InSAR Imaging of Aleutian Volcanoes: Monitoring a Volcanic Arc From Space*. *Springer, New York*.

Lu, Z., Wicks, C., Power, J. A., & Dzurisin, D. (2000). Ground deformation associated with the March 1996 earthquake swarm at Akutan volcano, Alaska, revealed by satellite radar interferometry. *Journal of Geophysical Research: Solid Earth*, *105*(B9), 21483–21495. https://doi.org/10.1029/2000jb900200

Lu, Z., Wicks, C., Kwoun, O., Power, J. A., & Dzurisin, D. (2005). Surface deformation associated with the March 1996 earthquake swarm at Akutan Island, Alaska, revealed by C-band ERS and L-band JERS radar interferometry. *Canadian Journal of Remote Sensing*, *31*(1), 7–20. https://doi.org/10.5589/m04-054

Mann, M., Kaspereit, D., & Kirkman, R. (2019). *Akutan Geothermal: Resource Report*. Golden, CO (United States). https://doi.org/10.2172/1596089

McConnell, V. S., Beget, J. E., Roach, A. L., Bean, K. W., & Nye, C. J. (1998). *Geologic map of the Makushin Volcanic Field, Unalaska Island, Alaska*. https://doi.org/10.14509/2576

Mercier, D., & Lowell, R. P. (2016). A quantitative analysis of volcanic unrest: Mt. Spurr Alaska, 2002-2006. *Journal of Volcanology and Geothermal Research*, *323*, 97–109. https://doi.org/10.1016/j.jvolgeores.2016.05.003

Miller, T. P., McGimsey, R. G., Richter, D. H., Riehle, J. R., Nye, C. J., Yount, M. E., & Dumoulin, J. A. (1998). Department of the Interior U . S . Geological Survey Catalog of the Historically Active Volcanoes of Alaska, 104. Retrieved from https://pubs.usgs.gov/of/1998/0582/report.pdf

Motyka, R. J., Wescott, E. M., Turner, D. L., Swanson, S. E., Romick, J. D., Moorman, M. A., & Allely, R. D. (1985). *Geological, geochemical, and geophysical survey of the geothermal resources at Hot Springs Bay Valley, Akutan Island, Alaska*. *Alaska Dept. of Natural Resources, Fairbanks (USA)* (Vol. 1). Alaska Division of Geological & Geophysical Surveys.

Murphy, R., Thurber, C., Prejean, S., & Bennington, N. (2014). Three-dimensional seismic velocity structure and earthquake relocations at Katmai, Alaska. *Journal of Volcanology and Geothermal Research*, *276*, 121–131. https://doi.org/10.1016/j.jvolgeores.2014.02.022

Myers, J. D., Marsh, B. D., & Sinha, A. K. (1985). Strontium isotopic and selected trace element variations between two Aleutian volcanic centers (Adak and Atka): implications for the development of arc volcanic plumbing systems. *Contributions to Mineralogy and*

Petrology, *91*(3), 221–234.

Nakajima, J., & Hasegawa, A. (2003). Tomographic imaging of seismic velocity structure in and around the Onikobe volcanic area, northeastern Japan: Implications for fluid distribution. *Journal of Volcanology and Geothermal Research*, *127*(1–2), 1–18. https://doi.org/10.1016/S0377-0273(03)00155-0

Neal, C. A, & McGimsey, R. G. (1997). 1996 Volcanic Activity in Alaska and Kamchatka : Summary of Events and Response. *U.S. Geological Survey Open-File Report 97-433*.

Nolet, G. (1987). Seismic wave propagation and seismic tomography. *Seismic Tomography*, 1–23. https://doi.org/10.1007/978-94-009-3899-1_1

Ohlendorf, S. J., Thurber, C. H., Pesicek, J. D., & Prejean, S. G. (2014). Seismicity and seismic structure at Okmok Volcano, Alaska. *Journal of Volcanology and Geothermal Research*, *278–279*, 103–119. https://doi.org/10.1016/j.jvolgeores.2014.04.002

Ohren, M., Bailey, A., Hinz, N., Oppliger, G., Hernandez, J., Rickard, W., & Dering, G. (2013). Akutan geothermal area exploration results and pre-drilling resource model. *Transactions - Geothermal Resources Council*, *37*(PART 1), 301–307.

Paige, C. C., & Saunders, M. A. (1982). LSQR: An algorithm for sparse linear equations and sparse least squares. *ACM Transactions on Mathematical Software (TOMS)*, *8*(2), 43–71. Retrieved from http://dl.acm.org/doi/10.1145/355993.356000

Pallister, J. S., McCausland, W. A., Jónsson, S., Lu, Z., Zahran, H. M., El Hadidy, S., et al. (2010). Broad accommodation of rift-related extension recorded by dyke intrusion in Saudi Arabia. *Nature Geoscience*, *3*(10), 705–712. https://doi.org/10.1038/ngeo966

Pellerin, C. L. M., & Christensen, N. I. (1998). Interpretation of crustal seismic velocities in the San Gabriel - Mojave region, southern California. *Tectonophysics*, *286*(1–4), 253–271. https://doi.org/10.1016/s0040-1951(97)00269-2

Power, J. A., Jolly, A. D., Page, R. A., & McNutt, S. R. (1995). Seismicity and forecastin of the 1992 Eruptions of Crater Peak Vent, Mount Spurr Volcano, Alaska: An overview. In T. E. C. Keith (Ed.), *The 1992 Eruptions of Crater Peak Vent, Mount Spurt Volcano, Alaska* (pp. 149–159).

Power, J. (2004). Renewed unrest at Mount Spurr Volcano, Alaska. *Eos*, *85*(43), 434.

https://doi.org/10.1029/2004EO430004

Power, J. A., Villaseñor, A., & Benz, H. M. (1998). Seismic image of the Mount Spurr magmatic system. *Bulletin of Volcanology*, *60*(1), 27–37. https://doi.org/10.1007/s004450050214

Power, J. A., Lahr, J. C., Page, R. A., Chouet, B. A., Stephens, C. D., Harlow, D. H., et al. (1994). Seismic evolution of the 1989-1990 eruption sequence of Redoubt Volcano, Alaska. *Journal of Volcanology and Geothermal Research*, *62*(1–4), 69–94. https://doi.org/10.1016/0377-0273(94)90029-9

Reeder, J. W. (1983). *Preliminary dating of the caldera forming Holocene volcanic events for the eastern Aleutian Islands*. *Geological Society of America Abstracts with Programs*.

Romick, J. D., Perfit, M. R., Swanson, S. E., & Shuster, R. D. (1990). Magmatism in the eastern Aleutian Arc: temporal characteristic of igneous activity on Akutan Island. *Contributions to Mineralogy and Petrology*, *104*(6), 700–721. https://doi.org/10.1007/BF01167288

Shapiro, N. M., Droznin, D. V., Droznina, S. Y., Senyukov, S. L., Gusev, A. A., & Gordeev, E. I. (2017). Deep and shallow long-period volcanic seismicity linked by fluid-pressure transfer. *Nature Geoscience*, *10*(6), 442–445. https://doi.org/10.1038/ngeo2952

Shinohara, H., Ohba, T., Kazahaya, K., & Takahashi, H. (2008). Origin of volcanic gases discharging from a cooling lava dome of Unzen volcano, Japan. *Journal of Volcanology and Geothermal Research*, *175*(1–2), 133–140. https://doi.org/10.1016/j.jvolgeores.2008.03.024

Siebert, L., & Simkin, T. (2013). Volcanoes of the world: An illustrated catalog of Holocene volcanoes and their eruptions. Retrieved from http://www.volcano.si.edu

Simkin, T., & Siebert, L. (1994). Volcanoes of the World. *Geoscience Press. Tucson*.

Stelling, P., Hinz, N. H., Kolker, A., & Ohren, M. (2015). Exploration of the Hot Springs Bay Valley (HSBV) geothermal resource area, Akutan, Alaska. *Geothermics*, *57*, 127–144. https://doi.org/10.1016/j.geothermics.2015.05.002

Sychev, I., Koulakov, I., El Khrepy, S., & Al-Arifi, N. (2017). Pathways of volatile migration in the crust beneath Harrat Lunayyir (Saudi Arabia) during the unrest in 2009 revealed by attenuation tomography. *Journal of Volcanology and Geothermal Research*, *330*, 1–13. https://doi.org/10.1016/j.jvolgeores.2016.12.002

Sychev, I. V., Koulakov, I., Egorushkin, I., Zhuravlev, S., West, M., El Khrepy, S., et al. (2019). Fault-Associated Magma Conduits Beneath Volcán de Colima Revealed by Seismic Velocity and Attenuation Tomography Studies. *Journal of Geophysical Research: Solid Earth*, *124*(8), 8908–8923. https://doi.org/10.1029/2019JB017449

Syracuse, E. M., Maceira, M., Zhang, H., & Thurber, C. H. (2015). Seismicity and structure of Akutan and Makushin Volcanoes, Alaska, using joint body and surface wave tomography. *Journal of Geophysical Research: Solid Earth*, *120*(2), 1036–1052. https://doi.org/10.1002/2014JB011616

Syracuse, E. M., Thurber, C. H., & Power, J. A. (2011). The Augustine magmatic system as revealed by seismic tomography and relocated earthquake hypocenters from 1994 through 2009. *Journal of Geophysical Research: Solid Earth*, *116*(9), 1–11. https://doi.org/10.1029/2010JB008129

Takei, Y. (2002). Effect of pore geometry on V P / V S : From equilibrium geometry to crack . *Journal of Geophysical Research*, *107*(B2). https://doi.org/10.1029/2001jb000522

Tokarev, P.I. (1984). The Asacha swarm of seismicity and its nature (Kamchatka, March 1983). *Volcanol. Seismol*, *3*, 3–13.

Um, J., & Thurber, C. (1987). A fast algorithm for two-point seismic ray tracing. *Bulletin of the Seismological Society of America*, *77*(3), 972–986.

Vargas, C. A., Koulakov, I., Jaupart, C., Gladkov, V., Gomez, E., El Khrepy, S., & Al-Arifi, N. (2017). Breathing of the Nevado del Ruiz volcano reservoir, Colombia, inferred from repeated seismic tomography. *Scientific Reports*, *7*(April), 8–13. https://doi.org/10.1038/srep46094

Waythomas, C. F. (1999). Stratigraphic framework of Holocene volcaniclastic deposits, Akutan Volcano, east-central Aleutian Islands, Alaska. *Bulletin of Volcanology*, *61*(3), 141–161. https://doi.org/10.1007/s004450050268

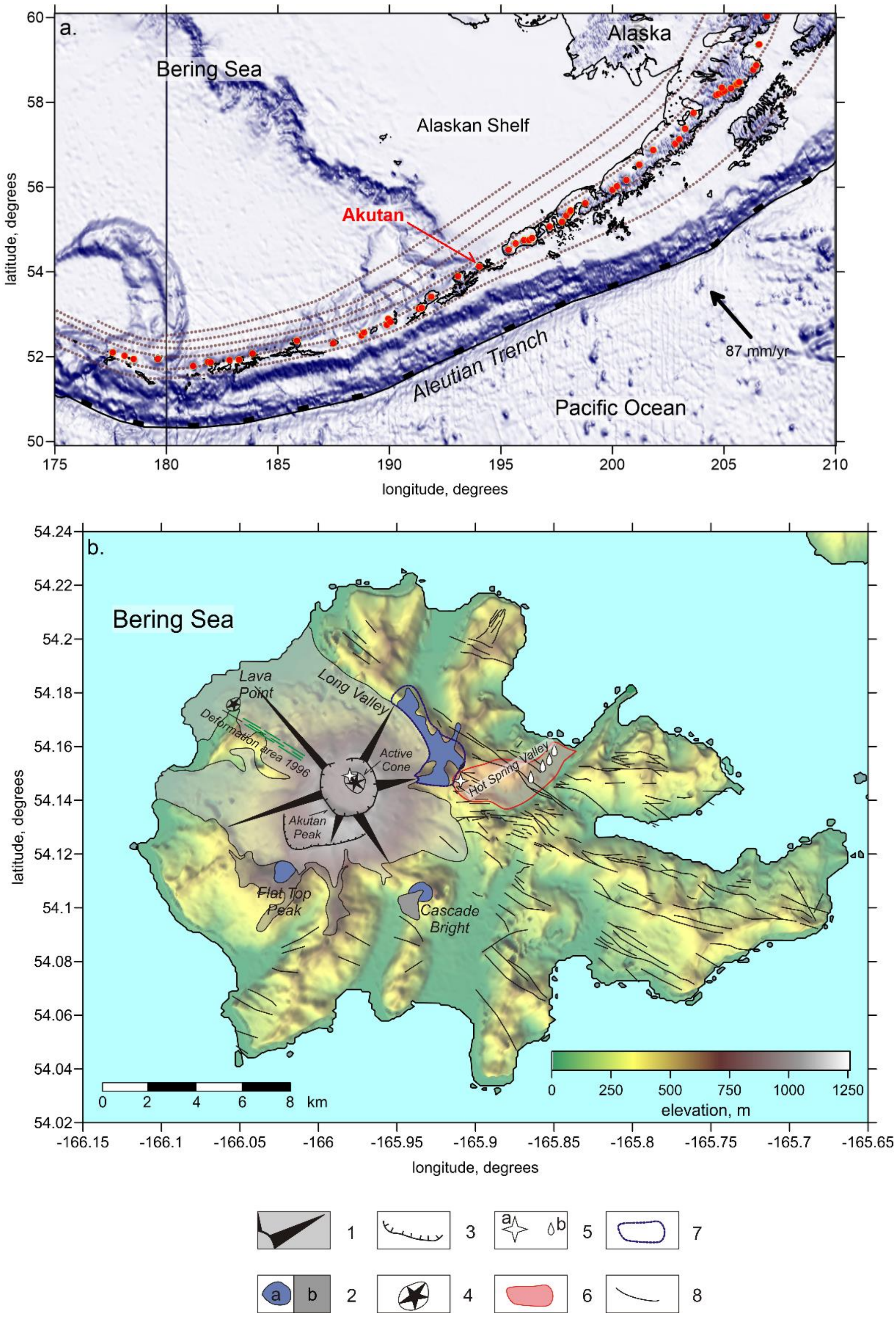

Figure 1. Study area. a. General view to the eastern part of the Aleutian arc and Alaska. Background is the shaded topography. Red dots are the Holocene volcanoes. Dotted lines indicate the dipping of the slab with the interval of 50 km. b. Topography and generalized geology of the Akutan Island by (Richter et al., 1998) with modifications: 1 - modern Akutan volcano with its lava flows and pyroclastic deposits; 2 - older subsidiary vents with lava plugs and breccia (a) and lava flows (b); 3 - caldera rims; 4 - scoria cones; 5 - flank fumarole field (a) and Hot Springs Bay Valley hot springs (b) ; 6 - active thermal spring and fumarole area (Ohren et al., 2013); 7 - inactive hydrothermal activity area (Mann, 2019); 8 - faults (Stelling et al., 2015).

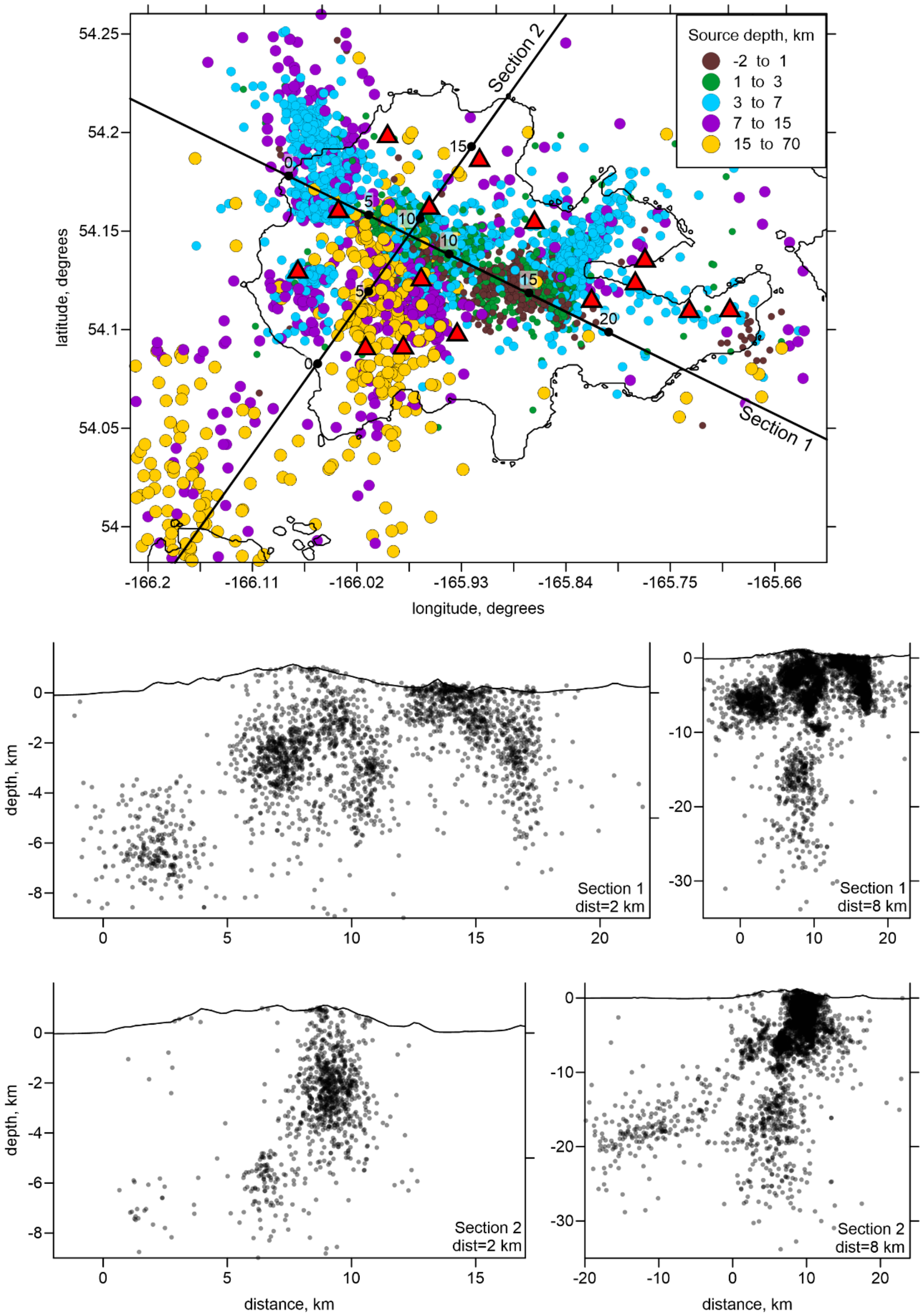

Figure 2. Locations of seismicity in map view (upper plot) and in two vertical sections. In map view, the colored dots represent the events classed by depth. Red triangles depict the seismic stations used in this study. For each vertical section, we present events in a shallower part (left row) and in a larger area (right row). Maximum distances from the events to the profile are indicated in captions at each plot.

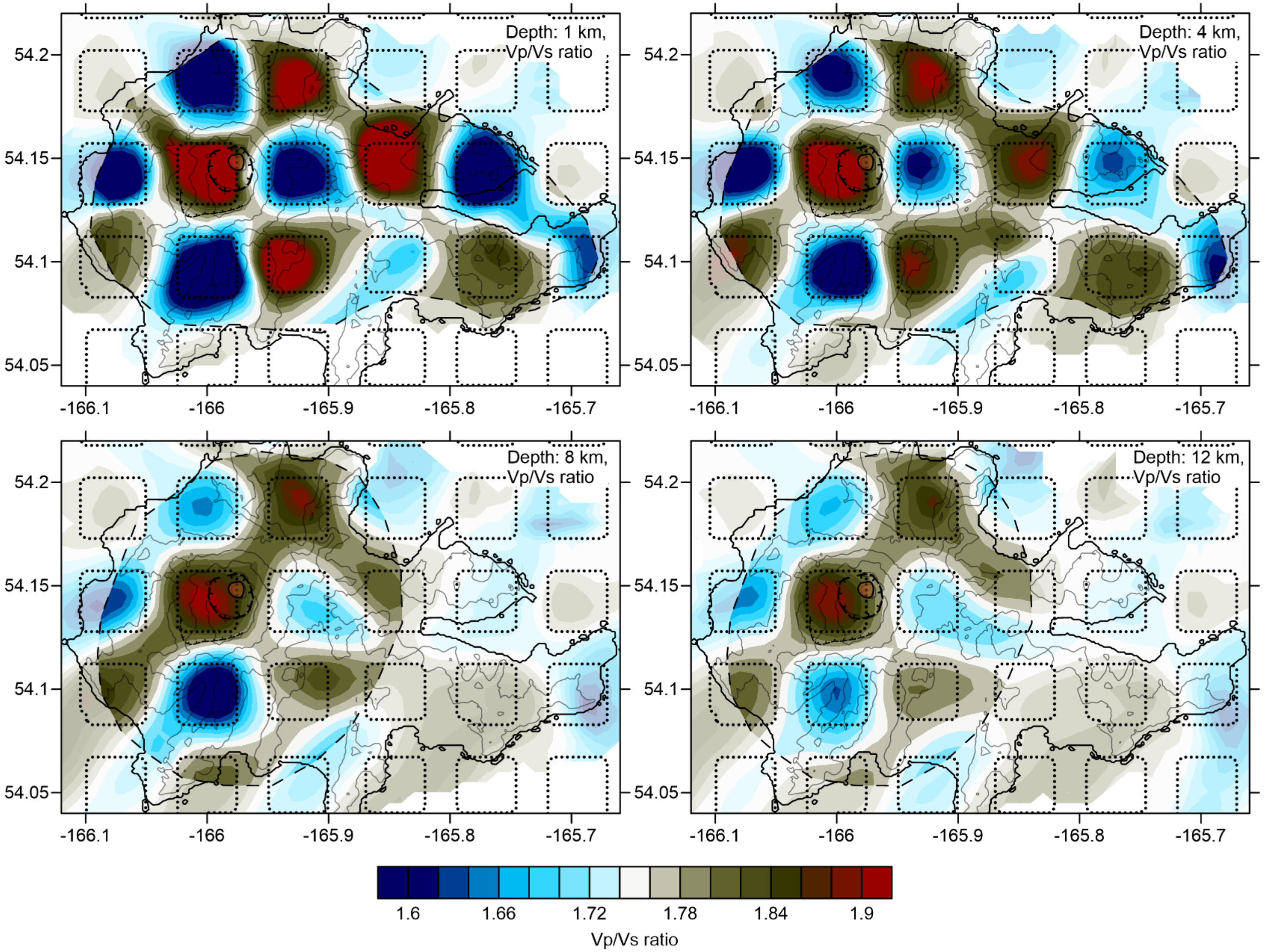

Figure 3. Checkerboard for testing the horizontal resolution, in which the synthetic anomalies do not change with depth. The dotted lines highlight the locations of the synthetic anomalies. Here, we show only the recovered distributions of the Vp/Vs ratio. Contour lines depict the topography with the interval of 200 m. The areas with poorer resolution are masked.

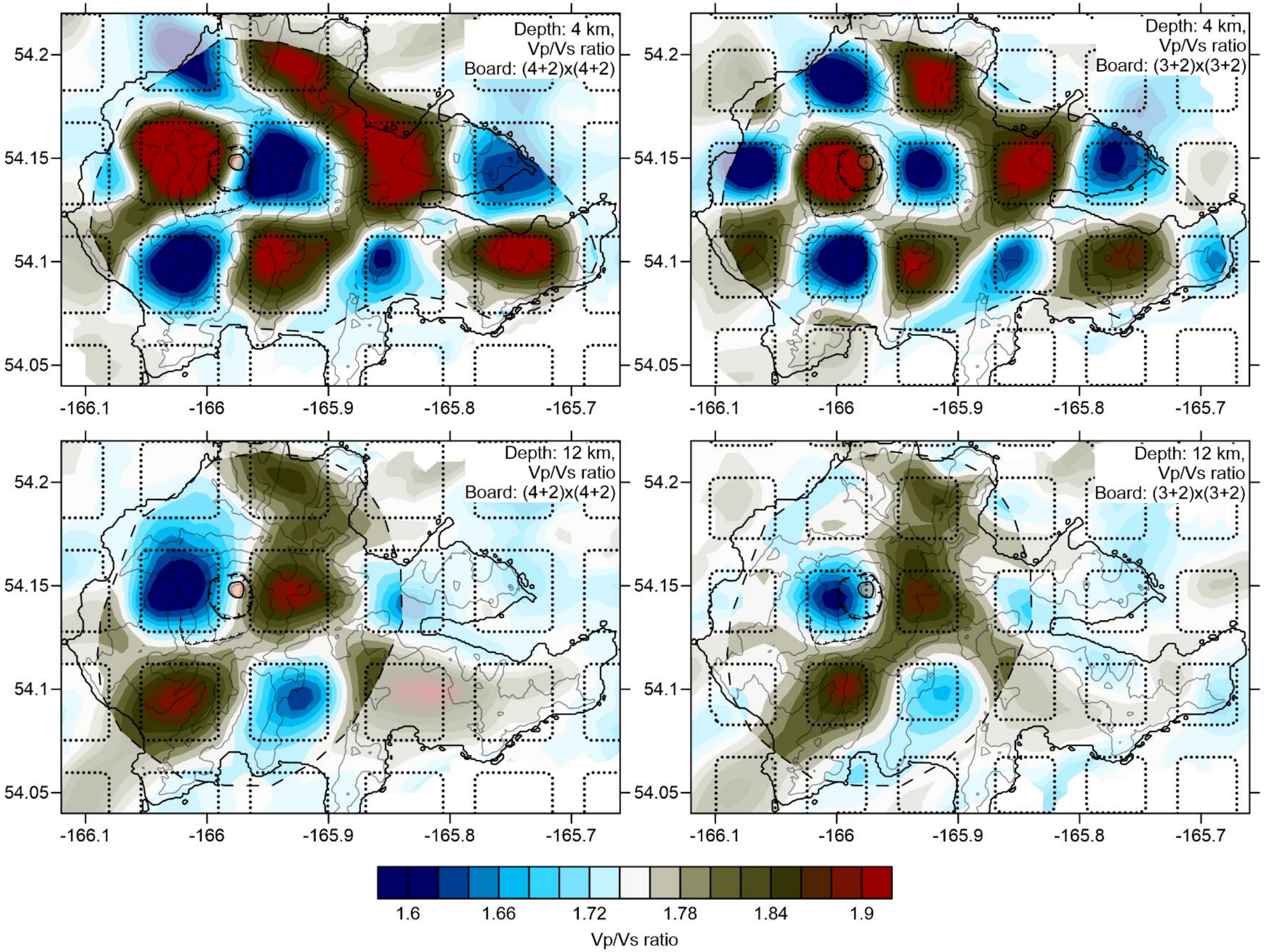

Figure 4. Checkerboard for testing the horizontal and vertical resolution. In this case, the sign of the synthetic anomalies changes in the depth interval from 6 to 8 km. The dotted lines highlight the locations of the synthetic anomalies. Here, we show only the recovered distributions of the Vp/Vs ratio. Contour lines depict the topography with the interval of 200 m. The areas with poorer resolution are masked.

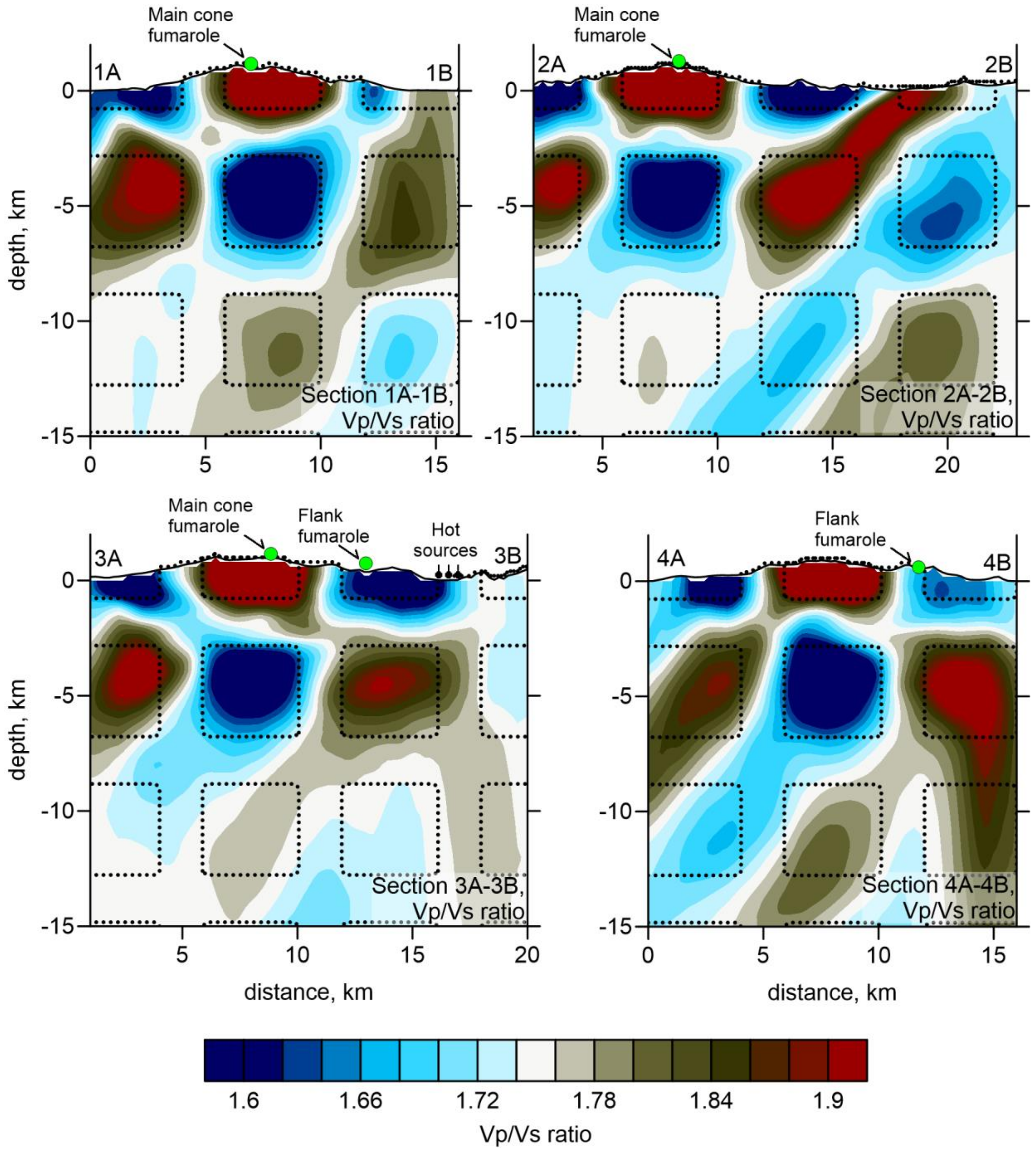

Figure 5. Synthetic tests for checking the vertical resolution. Each plot represents a separate model defined along one of four vertical sections. The recovered results are shown for the Vp/Vs ratio.

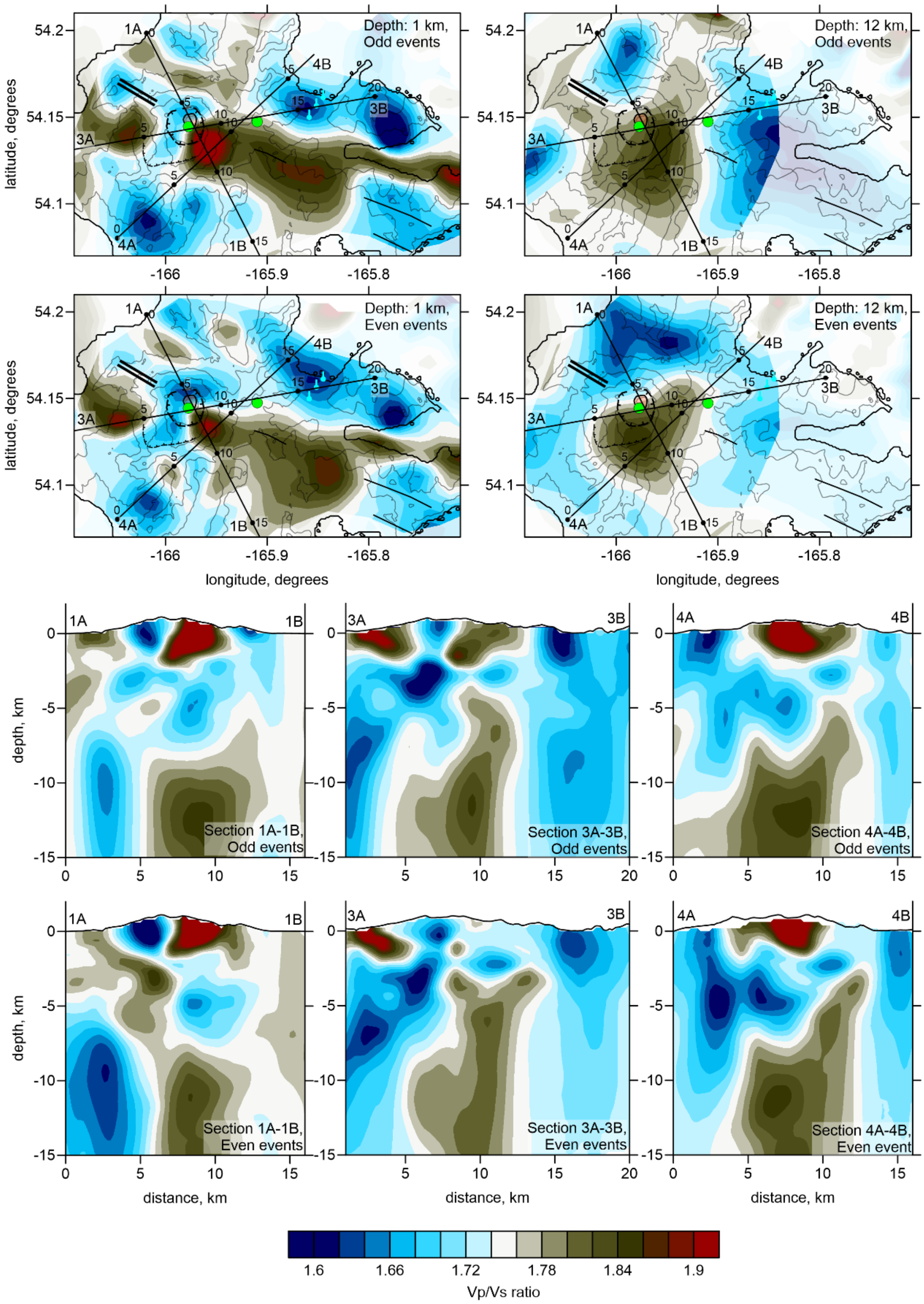

Figure 6. Odd/even test consisting in independent inversions of two subsets separated by a random criterion (with odd and even numbers of events). The resulting distributions of the Vp/Vs ratio are shown in two horizontal sections and three vertical sections.

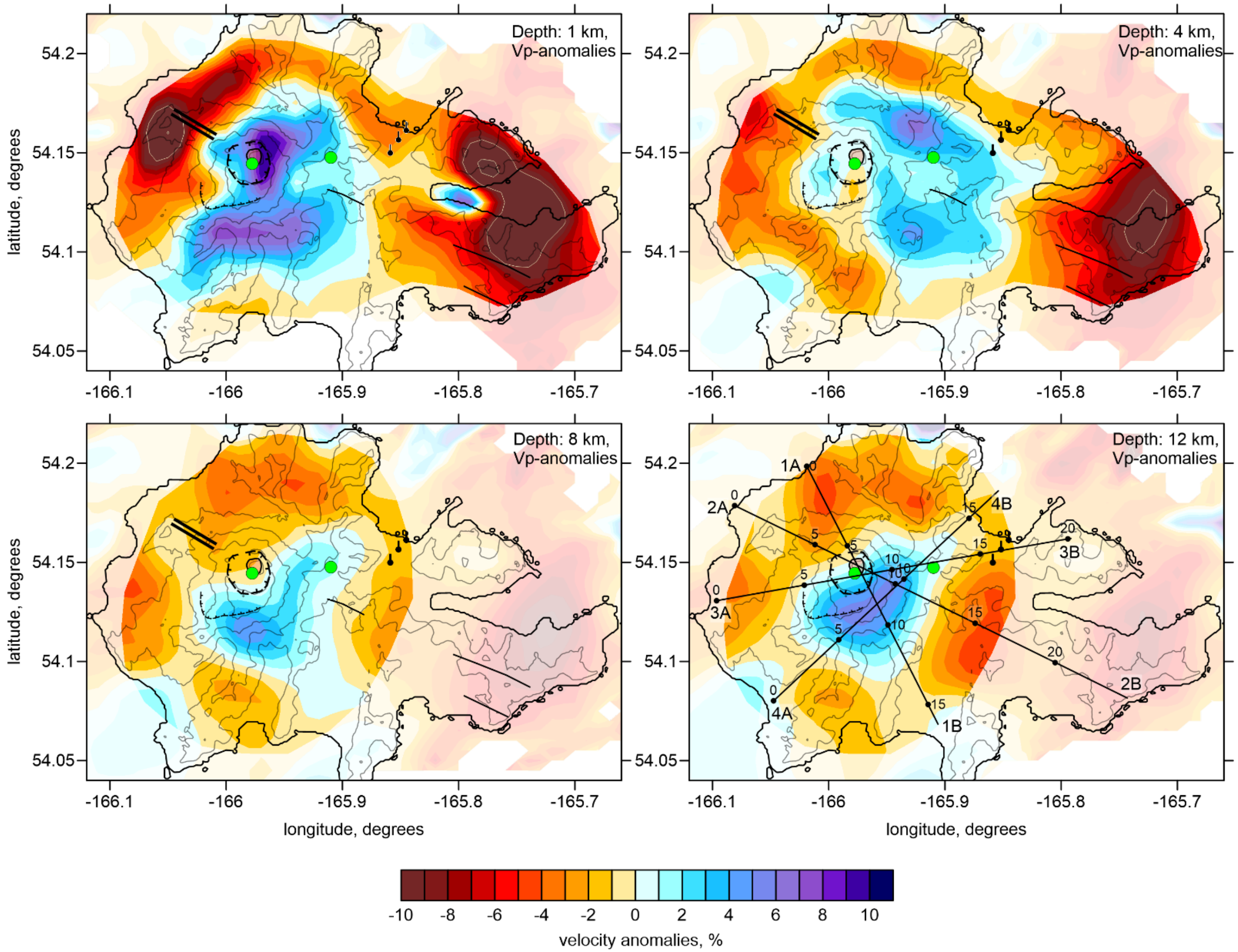

999

1000 Figure 7. P-wave velocity anomalies derived from the inversion of experimental data presented in four horizontal sections.

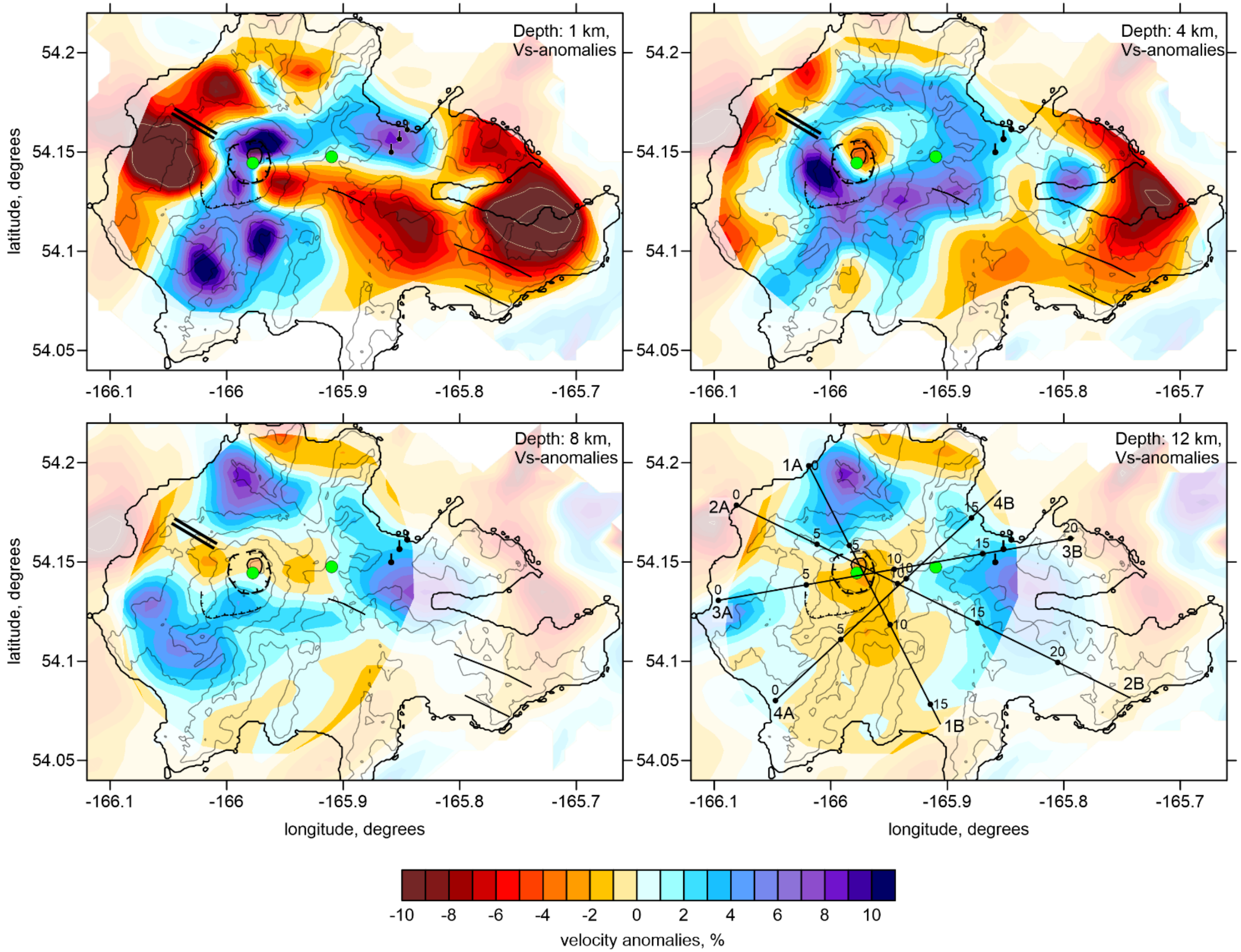

Figure 8. S-wave velocity anomalies derived from the inversion of experimental data presented in four horizontal sections.

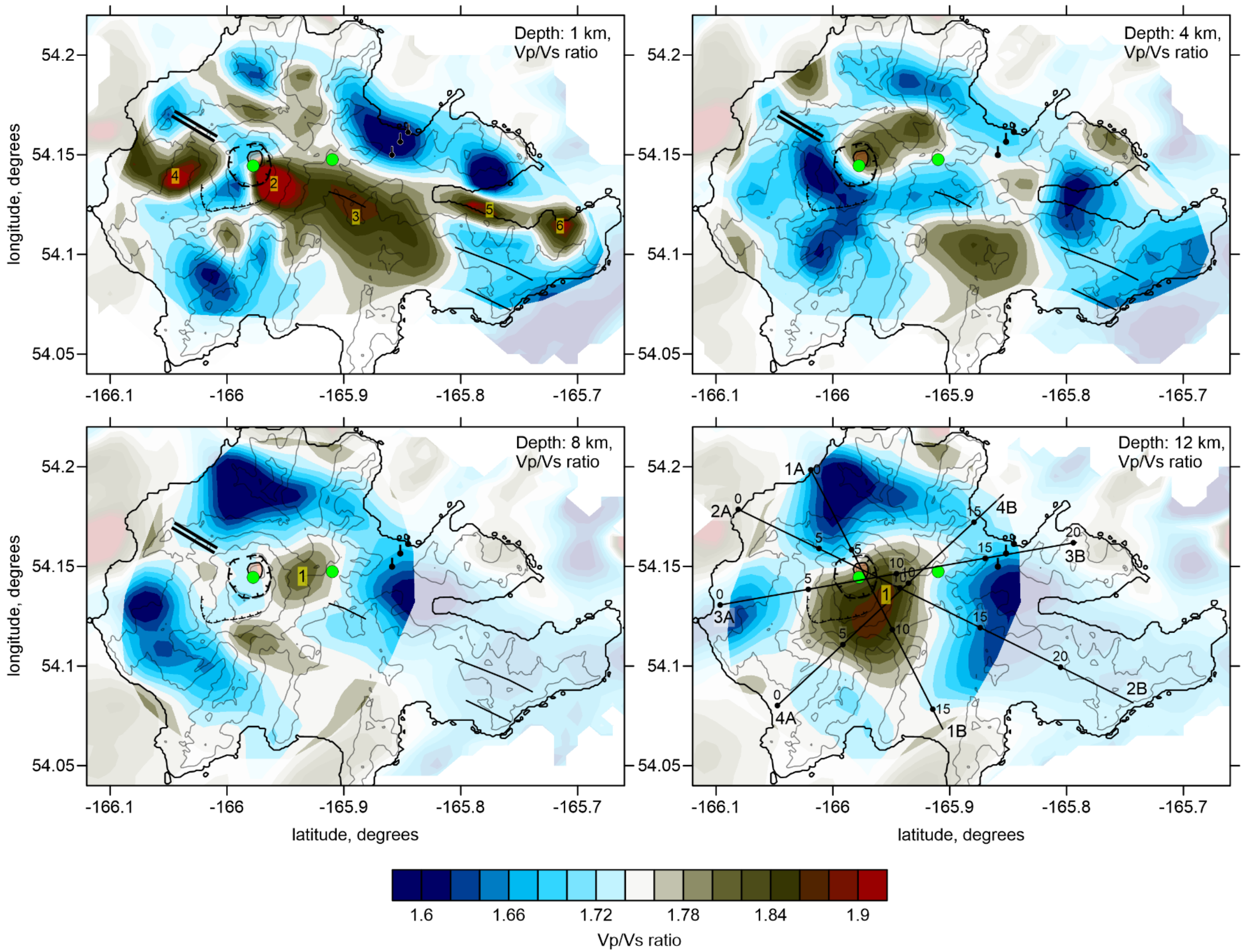

Figure 9. Vp/Vs ratio derived from the inversion of experimental data presented in four horizontal sections.

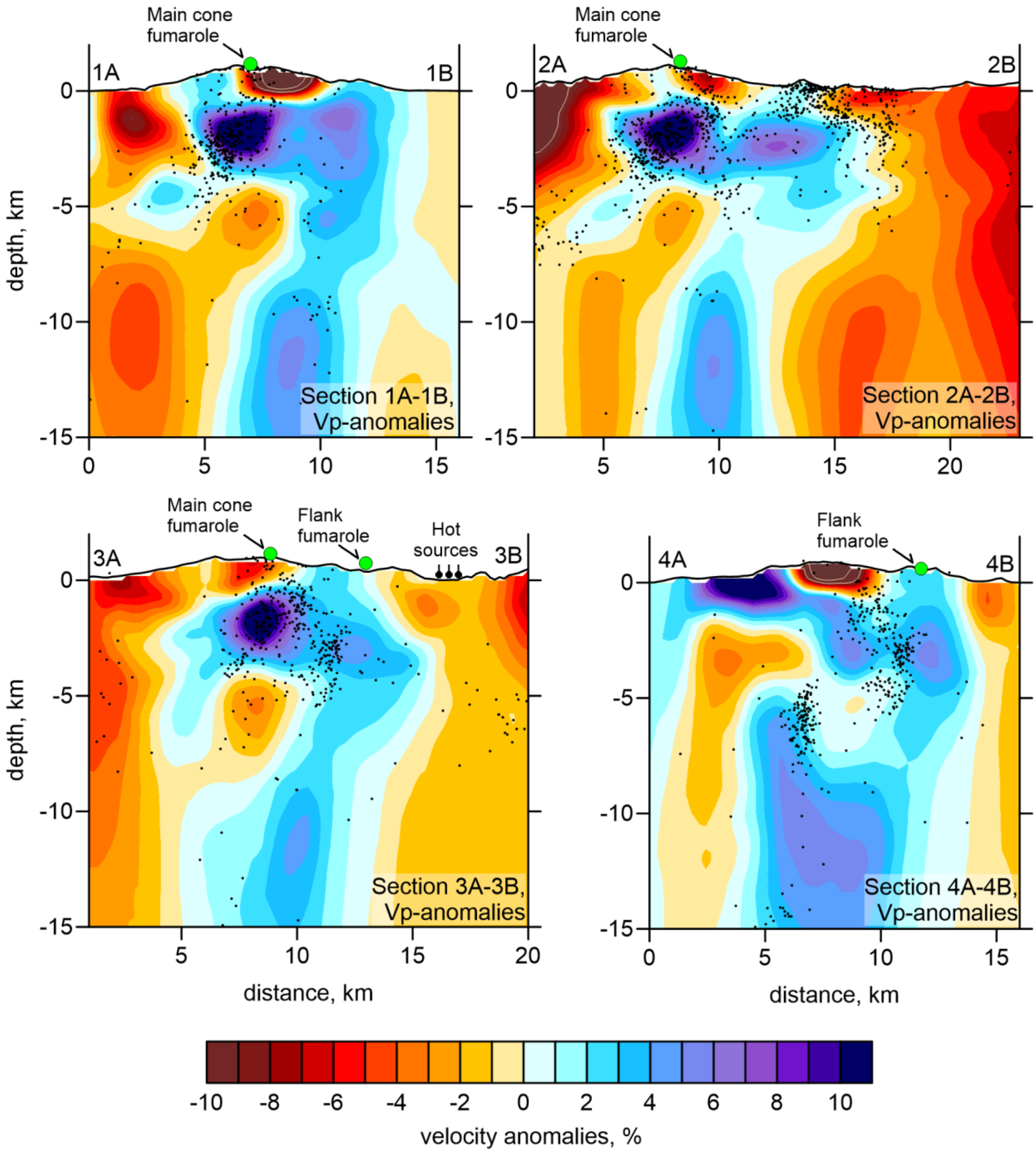

Figure 10. P-wave velocity anomalies derived from the inversion of experimental data presented in four vertical sections whose locations are indicated in Figures 7 to 9. Dots indicate the locations of the events at distances less than 1 km from the profile.

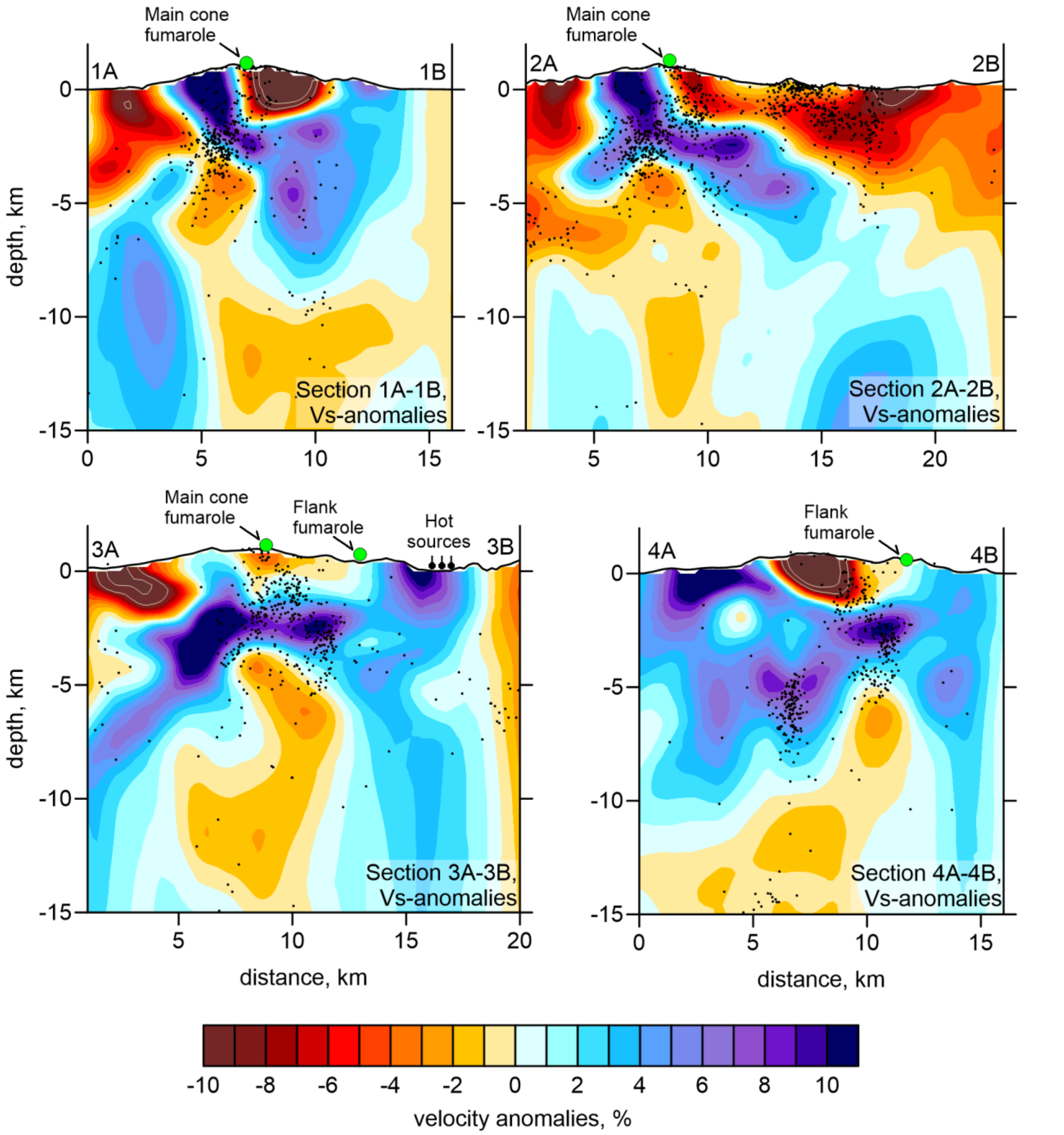

Figure 11. S-wave velocity anomalies derived from the inversion of experimental data presented in four vertical sections whose locations are indicated in Figures 7 to 9. Dots indicate the locations of the events at distances less than 1 km from the profile.

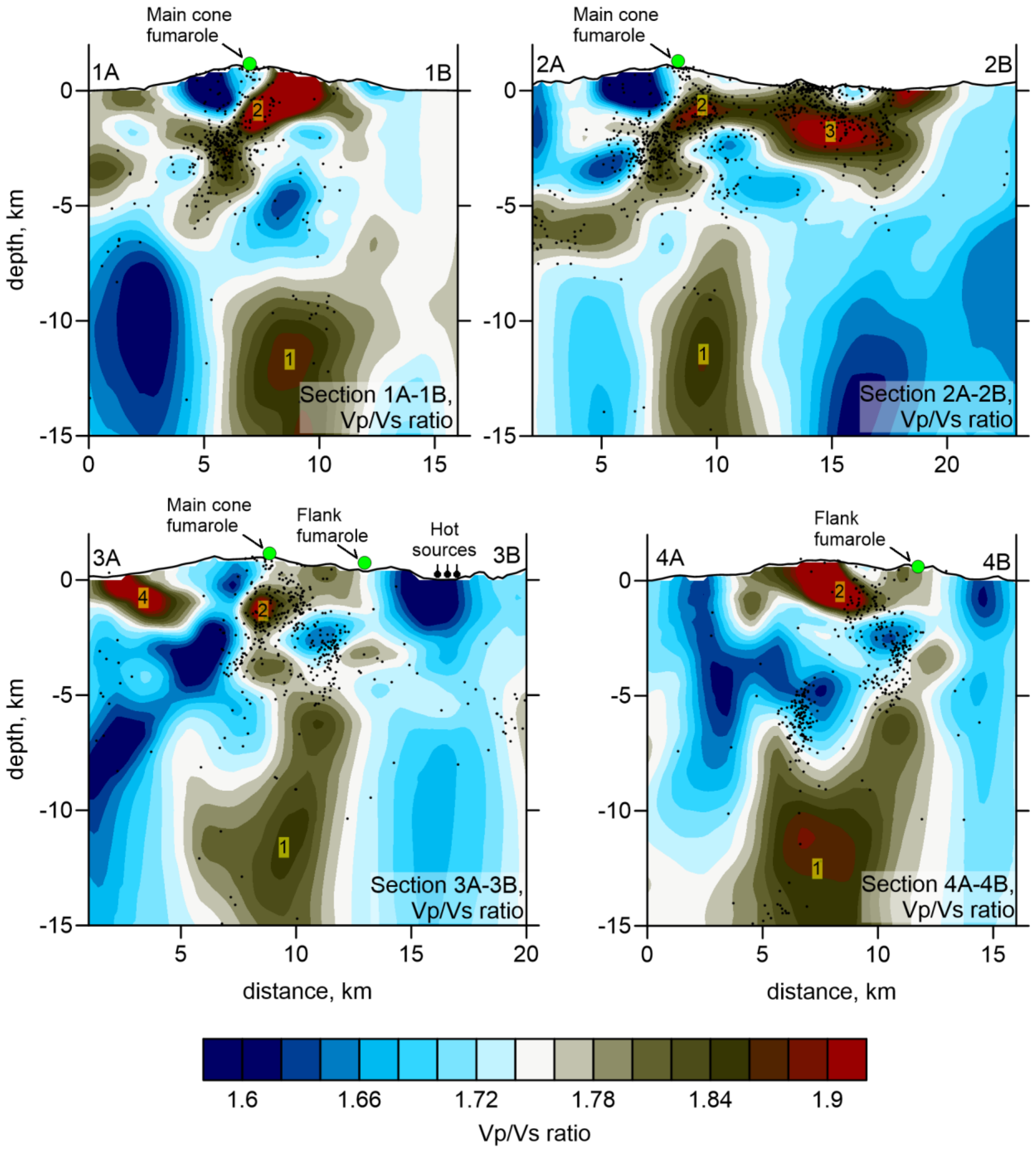

Figure 12. Vp/Vs ratio derived from the inversion of experimental data presented in four vertical sections whose locations are indicated in Figures 7 to 9. Dots indicate the locations of the events at distances less than 1 km from the profile.

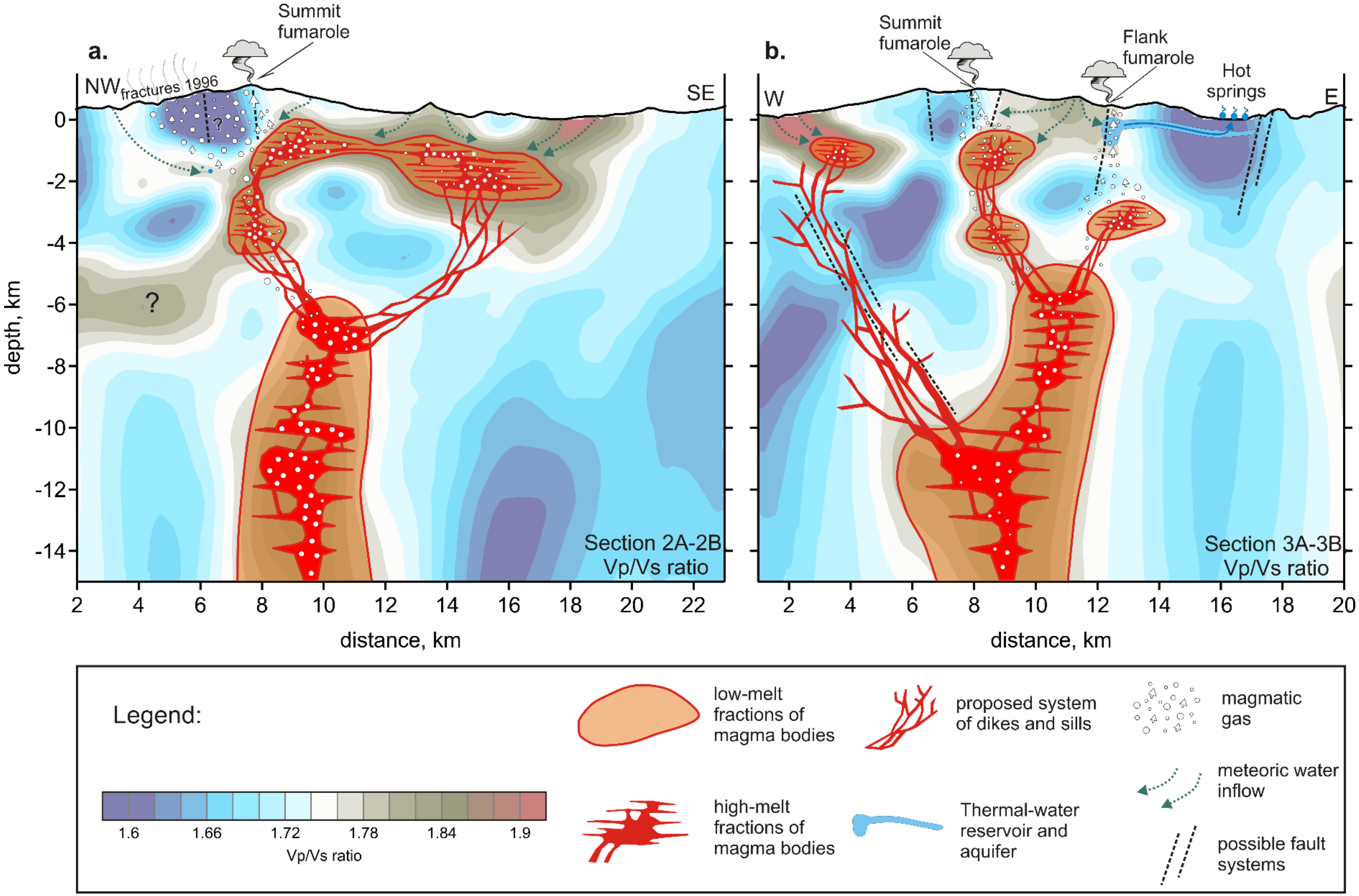

Figure 13. Schematic interpretation of the resulting distributions of the Vp/Vs ratio in vertical sections 2A-2B and 3A-3B, same as shown in Figure 12. See details in the text.